1   # CFD modelling of particle shrinkage in a fluidized bed for biomass fast

2   # pyrolysis with quadrature method of moment

3   Bo Liu[a], Konstantinos Papadikis[b], Sai Gu[c], Beatriz Fidalgo[a], Philip Longhurst[a], Zhongyuan Li[a] and

4   Athanasios Kolios[a]

5   a - Bioenergy and Resource Management Centre, Energy Theme, Cranfield University, College Road, Cranfield, Bedfordshire MK43 0AL, UK;

6   b - Department of Civil Engineering, Xi'an Jiaotong Liverpool University, 111 Ren'ai Road, Suzhou Dushu Lake Science and Education
7   Innovation District, Suzhou Industrial Park, Suzhou 215123, China;

8   c - Department of Chemical & Process Engineering, University of Surrey, Guildford, Surrey GU2 7XH, UK

9   **Abstract:**

10   An Eulerian-Eulerian multi-phase CFD model was set up to simulate a lab-scale fluidized bed reactor

11   for the fast pyrolysis of biomass. Biomass particles and the bed material (sand) were considered to be

12   particulate phases and modelled using the kinetic theory of granular flow. A global, multi-stage

13   chemical kinetic mechanism was integrated into the main framework of the CFD model and employed

14   to account for the process of biomass devolatilization. A 3-parameter shrinkage model was used to

15   describe the variation in particle size due to biomass decomposition. This particle shrinkage model

16   was then used in combination with a quadrature method of moment (QMOM) to solve the particle

17   population balance equation (PBE). The evolution of biomass particle size in the fluidized bed was

18   obtained for several different patterns of particle shrinkage, which were represented by different

19   values of shrinkage factors. In addition, pore formation inside the biomass particle was simulated for

20   these shrinkage patterns, and thus, the density variation of biomass particles is taken into account.

21   **Key words:**

22   Fluidized bed, biomass, fast pyrolysis, CFD, QMOM, particle shrinkage

1. Background

Among the various forms of renewable energy, biomass is becoming a promising resource for energy production, especially transportation fuel, as it has a huge potential for substituting fossil fuels on a large scale. This would relieve the strong dependency of mankind on the petroleum industry and contribute to tackling environmental problems, such as climate change and global warming. Biofuel production is currently based mainly on edible crops, i.e. starch and sugar in the case of bioethanol, and vegetable oils in the case of biodiesel. The use of food crops for the production of 1st generation biofuels may have negative effects on food production, including supply, prices and long term soil depletion [1]. In contrast, lignocellulosic biomass such as energy crops, forestry and agricultural residues, are a lower cost resource as these are not in direct competition with the food supply [2, 3]. Therefore, advanced bio-fuel technologies based on non-edible feed stocks are more attractive bio-based industry options for the future.

Bridgwater [4, 5] provides a comprehensive analysis of the thermal conversion of biomass from an economic and technical perspective. Thermal treatment, particularly pyrolysis and gasification, is potentially the most economic conversion process for producing biofuel in competition with oil-based derivatives for storage and use in transportation [6, 7]. Of these methods, fast pyrolysis of lignocellulosic biomass has considerable advantages for producing liquid bio-oil [8]. In the past two decades, intensive research studies on fast pyrolysis have resulted in the design of a series of different reactors such as ablative, auger, entrained flow, vacuum, rotating cone, bubbling fluidized bed and circulating fluidized bed, etc. [9]. Among these developments, fluidized bed reactors have been proven to have a high thermal efficiency and stable product quality as a result of their fast heating and excellent gas-solid mass transfer rate [10].

Biomass fast pyrolysis in a fluidized bed reactor is an extremely complex process as it involves a wide range of chemical and physical phenomena across multiple scales of time and space. Typical examples include descriptions of gas-solid two-phase flow and mixing, turbulent dispersion, mass and heat

48   transfer and heterogeneous reactions [11]. Studying such complex processes not only requires the

49   chemical mechanism of pyrolysis to be determined from the molecular level, but importantly coupling

50   this with the gaseous and particulate flow environment. Understanding the behaviour of biomass

51   particles in a fluidized bed is central to determining the product distribution in order to optimize the

52   bio-oil quality [12]. With the rapid development of computing capability, the cutting-edge CFD

53   (Computational Fluid Dynamics) method becomes a good alternative to take the place of traditional

54   experiments in studying the massive flow and decomposition of particles in a fluidized bed reactor.

55   Whilst there are still problems and challenges for multi-phase flow in CFD, especially multi-physics

56   processes, CFD gives acceptable predictions about the hydrodynamic characteristics of the fluidized

57   bed [13-15]. Within the past ten years, effort has been placed on developing comprehensive,

58   computational and predictive CFD models for biomass pyrolysis within fluidized bed reactors.

59   According to differing views on particle dynamics in a CFD framework, existing models can be classified

60   into two basic categories: the Eulerian method and the Lagrangian method. Models in both categories

61   give successful predictions on the general properties of fast pyrolysis in a fluidized bed, such as particle

62   motion, heat transfer and mass transfer, as well as rate of biomass conversion and product yield [16].

63   The Eulerian method is preferred by many researchers due to its low computing cost, good predictive

64   capability, and relative ease in computer programming. Hence, the Eulerian method has been widely

65   used in previous studies modelling fluidized bed reactors. Lathouwers and Bellan [17, 18] provide an

66   example of a comprehensive model based on Eulerian multi-phase fluid dynamics and the kinetic

67   theory of granular flow. They integrated the decomposition mechanism of biomass particles into their

68   CFD model to investigate the effects of operating parameters on product yields in a lab-scale fluidized

69   bed. Gerhauser *et al.* [19] carried out a more detailed modelling study focusing on the hydrodynamics

70   of the fluidized bed, whereas, Gerber *et al.* [20] set up an Eulerian-based model to simulate the

71   pyrolysis reactor with char particles as the fluidized medium so as to compare their numerical results

72   with experimental data. Xue *et al.* [21, 22] and Xue & Fox [12] developed a CFD model that accounts

73   for variations in biomass particle density caused by devolatilization. Their study assumes a continuous

74   loss of mass due to pyrolysis reactions making each particle more porous without changing its size.

75   Mellin *et al.* [23, 24] conducted a 3-D CFD simulation of a lab-scale fluidized bed and included a more

76   detailed prediction of gaseous and liquid product distribution by implementing a comprehensive

77   kinetic model of biomass pyrolysis proposed earlier by Ranzi *et al.* [25]. In contrast to Eulerian method

78   examples, Fletcher *et al.*'s [26] work is based on the Lagrangian approach. In this study, the motion of

79   the biomass particle is tracked by applying Newton's law, ignoring particle collision and employing a

80   global reaction mechanism to account for particle decomposition. Papadikis *et al.* [27-30] proposed a

81   method to simulate a single biomass particle in a pre-fluidized bed based on an Eulerian-Eulerian-

82   Lagrangian CFD framework. The parameters of particle motion, heat transfer between the particle and

83   the bed medium, internal heat conduction and reaction, and particle shrinkage, were systematically

84   studied. Bruchmuller *et al.* [31] tracked 0.8 million red oak particles inside a pyrolysis fluidized bed

85   reactor with the Lagrangian method and validated their model with experimental results.

86   Although a number of relatively detailed CFD models which describe the complex gas-solid reactive

87   flow in a bubbling fluidized bed for biomass fast pyrolysis have been developed, none of them

88   completely addresses all the chemical and physical phenomena involved due to the complexity of the

89   system itself. In general, researchers have focused their attention on defining the motion of particles

90   and their transport processes rather than their physical change and therefore the properties of

91   biomass particles within CFD models, e.g. porosity, size, and shape. Despite this, it is known that

92   biomass particles' changing size due to breakage and shrinkage occurs at high frequency during the

93   devolatilization process [18, 32-33, 34]. As a result, interactions between the biomass particle and the

94   bed medium are likely to change at the particle size and density changes. For example, the drag force

95   is directly affected, and consequently, the particle motion is likely to differ from cases where the size

96   and density changes are ignored; spatial distribution and the residence time of char particles in the

97   fluidized bed are also likely to be affected. The implication is that these changes are likely to impact

98   on secondary reaction sequences and the operating status of the reactor. It is this variation in size,

99   especially particle shrinkage, that is one of the most common phenomena of particle change during

100   the devolatilization process. The phenomenon of biomass shrinkage during the pyrolysis process has

101   been studied by several researchers [34, 35, 36-37]. The most notable work among these is the 3-

102   parameter shrinkage model proposed by Di Blasi. Despite this progress, the model can only be used

103   to predict the shrinkage of a single biomass particle at a given thermal condition but not the true

104   evolution of particle size in the complex reactor environment. Fan and Fox [13], Fan *et al.* [38, 39],

105   Marchisio & Fox [40] and Passalacqua *et al.* [41] propose a direct quadrature method of moment

106   (DQMOM) and combine this with the Eulerian multi-phase CFD model to describe the process of

107   particle mixing and segregation in a fluidized bed. Xue and Fox [12] further applied this method in

108   their CFD model to predict the distribution of biomass particle sizes in a bubbling fluidized bed during

109   fast pyrolysis. They argue that defining three quadrature abscissas guarantees a high accuracy in

110   determining the continuous particle size distribution; however, particle size variation was not taken

111   into account in this model.

112   In this paper, the Di Blasi 3-parameter particle shrinkage model is integrated into an Eulerian-based

113   multi-phase CFD framework in order to account for the evolution in particle size throughout the

114   fluidized bed. The quadrature method of moment (QMOM) is employed to solve the particle

115   population balance equation (PBE). This then determines the change in average particle diameter from

116   the biomass devolatilization. Differing shrinkage parameter values are used to represent differing

117   shrinkage patterns. These were investigated to find out how shrinkage affects the particle motion,

118   heating rate and the product yields. For the sake of simplicity, a multi-stage global kinetic model based

119   on pseudo-components was used to account for the chemical conversion of the biomass feed stock.

120   In addition to variation in particle size, the variation in density of the biomass was taken into account.

121   To best of our knowledge, no work similar to this has been reported that studies the size variation for

122   massive particle flow in the fluidized bed reactor during the fast pyrolysis of biomass.

2. Mathematical modelling

2.1 Governing equations

The basic idea underpinning the Eulerian model as it is used for multi-phase granular flow is to consider each phase, including the physical continuous and discrete phases, as interpenetrative fluids. Momentum equation of the solid phase is then closured with the kinetic theory in terms of models to calculate the solid viscosity and solid pressure. A detailed description of the multi-phase Eulerian model and kinetic theory can be found elsewhere in the multi-phase flow literature [42]. Table 1 gives a summary of the governing equations used in simulation of a fluidized bed reactor. Solid shear viscosity usually contains three main contributions, i.e. the collision viscosity, kinetic viscosity and frictional viscosity. In this study, collision viscosity is calculated according to Gidaspow et $al.$ [43], whilst kinetic viscosity is accounted for with the correlation of Syamlal et $al.$ [44]. Frictional viscosity is added due to high solid hold up and calculated with the model proposed by Schaeffer [45] using an internal frictional angle of 55 [12]. The radial distribution function $g_{0,ss}$ and the solid pressure p_s are calculated according to Lun et $al.$ [46]. The restitution coefficient e_{ss} takes the value of 0.9. The solid granular temperature Θ_s is calculated with the correlation proposed by Syamlal et $al.$ [44]. For multi-phase flow problems, momentum interactions between each pair of phases arises due to the drag force, which contributes as a source term $R_{i,j}$ in the phase momentum equations. A widely used drag model proposed by Gidaspow et $al.$ [43] is employed to calculate the gas-solid phase interaction coefficient $K_{i,j}$. The Syamlal-O'Brien-Symmetric model [47] is then used to calculate the drag coefficient between the biomass particles and the sand phase.

Table 1 Governing equations of the fluidized bed reactor based on Eulerian-Granular theory

	Models and equations
Continuity Gas	$$\frac{\partial \varepsilon_l \rho_l}{\partial t} + \nabla \cdot \left(\varepsilon_l \rho_l \mathbf{u}_l \right) = \sum_{j=1, j \neq l}^{3} \left(m_{j,l} - m_{l,j} \right) + S_l$$
Solid (sand/biomass)	$$\frac{\partial \varepsilon_i \rho_i}{\partial t} + \nabla \cdot \left(\varepsilon_i \rho_i \mathbf{u}_i \right) = \sum_{j=1, j \neq i}^{3} \left(m_{j,i} - m_{i,j} \right) + S_i \quad i=2, 3$$

Momentum

Gas

$$\frac{\partial \varepsilon_1 \rho_1 \mathbf{u}_1}{\partial t} + \nabla \cdot \left(\varepsilon_1 \rho_1 \mathbf{u}_1 \mathbf{u}_1 \right) = -\varepsilon_1 \nabla p + \nabla \cdot \overline{\overline{\tau}}_1 + \sum_{j=1, j \neq 1}^{3} \left(\mathbf{R}_{1,j} + m_{j,1} \mathbf{u}_{j,1} - m_{1,j} \mathbf{u}_{1,j} \right) + \varepsilon_1 \rho_1 g$$

$$\overline{\overline{\tau}}_1 = \varepsilon_1 \mu_1 \left(\nabla \mathbf{u}_1 + \nabla \mathbf{u}_1^\mathbf{T} \right) - \frac{2}{3} \varepsilon_1 \mu_1 \nabla \cdot \mathbf{u}_1 \overline{\overline{I}} \; ; \quad \mathbf{R}_{1,j} = K_{1,j} \left(\mathbf{u}_j - \mathbf{u}_1 \right)$$

Solid (sand/biomass)

$$\frac{\partial \varepsilon_i \rho_i \mathbf{u}_i}{\partial t} + \nabla \cdot \left(\varepsilon_i \rho_i \mathbf{u}_i \mathbf{u}_i \right) = -\varepsilon_i \nabla p - \nabla p_i + \nabla \cdot \overline{\overline{\tau}}_i + \sum_{j=1, j \neq i}^{3} \left(\mathbf{R}_{i,j} + m_{j,i} \mathbf{u}_{j,i} - m_{i,j} \mathbf{u}_{i,j} \right) + \varepsilon_i \rho_i g$$

$$\overline{\overline{\tau}}_i = \varepsilon_i \mu_i \left(\nabla \mathbf{u}_i + \nabla \mathbf{u}_i^\mathbf{T} \right) + \varepsilon_i \left(\lambda_i - \frac{2}{3} \mu_i \right) \nabla \cdot \mathbf{u}_i \overline{\overline{I}} \quad i=2, 3; \quad \mathbf{R}_{i,j} = K_{i,j} \left(\mathbf{u}_j - \mathbf{u}_i \right)$$

Granular kinetic models

Solid shear viscosity

$$\mu_s = \mu_{s,col} + \mu_{s,kin} + \mu_{s,fr}$$

Collision viscosity

$$\mu_{s,col} = \frac{4}{5} \varepsilon_s^2 \rho_s d_s g_{0,ss} \left(1 + e_{ss} \right) \sqrt{\frac{\Theta_s}{\pi}}$$

Kinetic viscosity

$$\mu_{s,kin} = \frac{\varepsilon_s \rho_s d_s \sqrt{\Theta_s \pi}}{6 \left(3 - e_{ss} \right)} \left[1 + 0.4 \left(1 + e_{ss} \right) \left(3 e_{ss} - 1 \right) \varepsilon_s g_{0,ss} \right]$$

Frictional viscosity

$$\mu_{s,fr} = \frac{p_s \sin \phi}{2 \sqrt{I_{2D}}}$$

Solid bulk viscosity

$$\lambda_s = \frac{4}{3} \varepsilon_s \rho_s d_s g_{0,ss} \left(1 + e_{ss} \right) \sqrt{\frac{\Theta_s}{\pi}}$$

Radial distribution function

$$g_{0,ss} = \left[1 - \left(\frac{\varepsilon_s}{\varepsilon_{s,max}} \right)^{1/3} \right]^{-1}$$

Solid pressure

$$p_s = \varepsilon_s \rho_s \Theta_s + 2 \rho_s \left(1 + e_{ss} \right) \varepsilon_s^2 g_{0,ss} \Theta_s$$

Granular temperature

$$\frac{3}{2} \left[\frac{\partial}{\partial t} \left(\rho_s \varepsilon_s \Theta_s \right) + \nabla \cdot \left(\rho_s \varepsilon_s \Theta_s \right) \right] = \left(-p_s \overline{\overline{I}} + \overline{\overline{\tau}}_s \right) : \nabla \mathbf{u}_s + \nabla \cdot \left(k_{\Theta_s} \nabla \Theta_s \right) - \gamma_{\Theta_s} + \varphi_{g,s}$$

Collision dissipation energy

$$\gamma_{\Theta_s} = \frac{12 \left(1 - e_{ss}^2 \right) g_{0,ss}}{d_s \sqrt{\pi}} \rho_s \varepsilon_s^2 \Theta_s^{3/2}$$

Transfer of kinetic energy

$$\varphi_{g,s} = -3 K_{g,s} \Theta_s$$

Species transport

$$\frac{\partial \varepsilon_i \rho_i x_{i,p}}{\partial t} + \nabla \cdot \left(\varepsilon_i \rho_i \mathbf{u}_i x_{i,q} \right) = \nabla \cdot \left(\varepsilon_i D_{i,q} \nabla x_{i,q} \right) + \Re_{i,q} + \sum_{j=1}^{N} \left(m_{j^p,i^q} - m_{i^q,j^p} \right) + \varepsilon_i S_{i,q} \quad i=1, 3$$

Energy

$$\frac{\partial \varepsilon_i \rho_i h_i}{\partial t} + \nabla \cdot \left(\varepsilon_i \mathbf{u}_i \rho_i h_i \right) = \varepsilon_i \frac{\partial p}{\partial t} + \overline{\overline{\tau}}_i : \nabla \mathbf{u}_i + \sum_{j=1, j \neq i}^{3} \left(\mathbf{R}_{i,j} \cdot \mathbf{u}_i + Q_{i,j} + m_{j,i} h_j - m_{i,j} h_i \right)$$

$$+ \nabla \cdot \left(\lambda_i \nabla T \right) + S_i$$

144

145   Note: Phase index i, j: 1 – gas phase; 2 - sand phase; 3 – biomass phase

146   Species transport equation and energy equation are solved based on each phase. Among all of the

147   energy sources, interphase heat transfer and the release of heat from chemical reactions are the most

148   significant energy sources from the fast pyrolysis of biomass in a fluidized bed. Table 2 gives the

149   thermodynamic parameters used in this work. Interphase heat transfer in a biomass fast pyrolysis

150   fluidized bed is extremely complex due to a variety of different physical heat transfer processes

151   occurring simultaneously, such as gas-solid convective heat transfer, solid-solid conductive heat

152   transfer and radiative heat transfer. Thus far, no work has been done to account for all these heat

153   transfer processes in a single mathematical model. Most of the existing studies are concerned mainly

154   with the gas-solid heat transfer which is likely to be dominant in particle heating. In this study, the

155   conductive and radiative heat transfer effects of the sand phase are not taken into account. A well-

156   known Nusselt correlation proposed by Gunn [48] was employed in this work to account for interphase

157   heat transfer between the fluidizing gas and the sand phase. Since the volumetric concentration of

158   the biomass phase is very low throughout the fluidized bed, existence of the biomass particles can be

159   ignored when calculating the gas-sand heat transfer coefficient. Heat transfer between the biomass

160   particles and the bed medium was calculated according to Collier *et al.* [49], who proposed a modified

161   Nusselt correlation in their studies on heat transfer between a free-moving bronze sphere and the

162   dense fluidizing medium (gas and inert particles). They argue that gas-solid heat transfer is dominant

163   when the heat transfer sphere is smaller than the bed particles, which is exactly the case in the current

164   study.

165
$$Nu = 2 + 0.9\,\mathrm{Re}^{0.62}(d_b / d_s)^{0.2}$$
(1)

166   Where, d_b is the diameter of the biomass particle; d_s is the diameter of the sand particle.

167   **Table 2 Thermodynamic parameters used in the simulation**

Species	C_p (kJ·kg^{-1}·K^{-1})		λ (W·m^{-1}·K^{-1})	
Cellulose, activated cellulose	2.3	[50]	0.2426	[50]
Hemicellulose, activated hemicellulose	2.3	[50]	0.2426	[50]
Lignin, activated lignin	2.3	[50]	0.2426	[50]
Char	1.1	[50]	0.1046	[51]
Tar	2.5	[50]	0.02577	[52]
Gas, void	1.1	[51]	0.02577	[51]
Nitrogen	1.091	[27]	0.0563	[27]
Sand	830	[24]	0.25	[24]

168

169

170   2.2 Chemical kinetic model of the biomass decomposition

171   Since this paper focuses mainly on demonstrating a method to describe the particle density

172   and size change in a fluidized bed reactor, rather than accurately predicting product yields, a

173   global chemical kinetic mechanism satisfies the current model in accounting for the biomass

174   devolatilization process. Shafizadeh and Bradbury [53] argue that, in the process of cellulose

175   pyrolysis, an activated intermediate is first produced, then two competitive conversion routes

176   occur afterwards, one which produces condensable bio-oil, and the other which gives

177   permanent gas and char. Ward and Braslaw [54], Koufopanos *et al.* [55], and Miller and Bellan

178   [56] extend this mechanism to the other main components of lignocellulosic biomass –

179   hemicellulose and lignin, and thus obtain a collective kinetic mechanism for biomass pyrolysis,

180   see Figure 1.
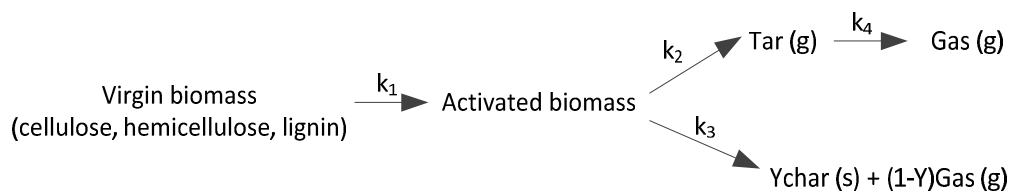
181

182   **Fig. 1 A multi-stage global reaction mechanism of biomass fast pyrolysis**

183   The biomass feedstock used in this work was assumed to be composed of 41wt.% cellulose,

184   32wt.% hemicellulose, and 27wt.% lignin. This is a typical woody biomass composition [57].

185   Chemical reactions 1-4 from Figure 1 are first-order Arrhenius reactions with respect to the

186   corresponding reactant. The kinetic parameters are shown in Table 3, where *Y* value in

187   reaction 3 depends on the specific components.

188   **Table 3 Kinetic parameters and reaction heat of biomass pyrolysis**

Reaction	Y	A (s^{-1})	E (kJ·mol^{-1})	$k_{T=773K}$ (kg·m^{-3}·s^{-1})		Δh (kJ·kg^{-1})	
$k_{1,c}$		2.8×10^{19}	242.4	539.246	[53]	0	[50]
$k_{2,c}$		3.28×10^{14}	196.5	8.775	[53]	255	[58]
$k_{3,c}$	0.35	1.3×10^{10}	150.5	0.5232	[53]	-20	[58]
$k_{1,h}$		2.1×10^{16}	186.7	2670.041	[54]	0	[58]
$k_{2,h}$		8.75×10^{15}	202.4	91.597	[56]	255	[58]

$k_{3,h}$	0.6	2.6×10^{11}	145.7	22.450	[56]	-20	[58]
$k_{1,l}$		9.6×10^{8}	107.6	35.493	[54]	0	[58]
$k_{2,l}$		1.5×10^{9}	143.8	0.175	[56]	255	[58]
$k_{3,l}$	0.75	7.7×10^{6}	111.4	0.156	[56]	-20	[58]
k_{4}		4.28×10^{6}	108.0	0.147	[59]	-42	[50]

Note: subscript c represents cellulose; h represents hemicellulose; l represents lignin.

The continuous loss of particle mass from devolatilization makes the biomass particles shrink and become more porous. Pore formation plays an important role in the apparent density change of the biomass particle. It is assumed that pores which form inside the biomass particle fill with permanent gas produced by the decomposition process. In other words, the majority of permanent gas produced is released to the gas phase, and a small fraction remains in the biomass particle, forming pores. Indeed, biomass particles maintain a very small holdup within the fluidized bed [21, 23], so the total amount of permanent gas inside the pores is extremely small and can be ignored when compared with the counterpart released to the gas phase. Therefore, this assumption incurs no significant artificial errors and provides a simple way to account for the apparent density change. The apparent density of the biomass particle is defined as the volume-weighted-average density of the component true densities, including virgin biomass, activated biomass, char, and permanent gas in pores that constitute the particle.

$$\rho_{apparent} = \left(\sum_{q=1}^{N} \frac{x_q}{\rho_q} \right)^{-1} \tag{2}$$

Where, x_q is the mass fraction of the qth component in the biomass phase, which has exactly the same meaning as $x_{3,q}$ in the species equation; ρ_q is the true density of the qth component. All phases and species involved in the current CFD model were numbered as shown in Table 4. Only n-1 transport equations were actually solved for each phase which contains n species in all. The nth component mass fraction can be derived directly from the law of unity: $x_{i,n} = 1 - \sum_{k=1}^{n-1} x_{i,k}$.

Table 4 Reference number of species in gas and biomass phase

Phases and components	Phase No.	Component No. in each phase
Gas phase	1	
Tar		1
Gas		2
N_2		3
Sand phase	2	
Sand		-

Biomass phase	3	
Char		1
Activated-lignin		2
Activated-hemicellulose		3
Activated-cellulose		4
Lignin		5
Hemicellulose		6
Cellulose		7
Void		8
Ash		9

209

210 Source terms $R_{i,q}$ referred to in the species transport equation can be calculated according to the

211 reaction mechanism and kinetic data provided in Figure 1 and Table 3, respectively. The numbering

212 criteria summarized in Table 4 are applied to subscripts i and q in the species transport equation, and

213 the reaction source term $R_{i,q}$ for each species can be written as follows.

214 **Table 5 Source terms of the species transport equations due to chemical reactions**

$$\Re_{1,1} = \rho_3\varepsilon_3 k_{2,c} x_{3,4} + \rho_3\varepsilon_3 k_{2,h} x_{3,3} + \rho_3\varepsilon_3 k_{2,l} x_{3,2} - \rho_1\varepsilon_1 k_4 x_{1,1}$$

$$\Re_{1,2} = \rho_3\varepsilon_3 k_{3,c}(1-Y_c) x_{3,4} + \rho_3\varepsilon_3 k_{3,h}(1-Y_h) x_{3,3} + \rho_3\varepsilon_3 k_{3,l}(1-Y_l) x_{3,2} + \rho_1\varepsilon_1 k_4 x_{1,1}$$

$$\Re_{3,1} = \rho_3\varepsilon_3 k_{3,c} Y_c x_{3,4} + \rho_3\varepsilon_3 k_{3,h} Y_h x_{3,3} + \rho_3\varepsilon_3 k_{3,l} Y_l x_{3,2}$$

$$\Re_{3,2} = \rho_3\varepsilon_3 k_{1,c} x_{3,5} - \rho_3\varepsilon_3 k_{2,c} x_{3,2}$$

$$\Re_{3,3} = \rho_3\varepsilon_3 k_{1,h} x_{3,6} - \rho_3\varepsilon_3 k_{2,c} x_{3,3}$$

$$\Re_{3,4} = \rho_3\varepsilon_3 k_{1,c} x_{3,7} - \rho_3\varepsilon_3 k_{2,c} x_{3,4}$$

$$\Re_{3,5} = -\rho_3\varepsilon_3 k_{1,l} x_{3,5}$$

$$\Re_{3,6} = -\rho_3\varepsilon_3 k_{1,h} x_{3,6}$$

$$\Re_{3,7} = -\rho_3\varepsilon_3 k_{1,c} x_{3,7}$$

215

216 It can be noted in Table 5 that none of the above expressions account for the mass fraction of the

217 component "void" which represents the quantity of pores formed in a devolatilizing biomass particle.

218 Only $R_{1,2}$ gives the total amount of permanent gas produced per unit volume per unit time, in place of

219 an exact distribution ratio for that released to the gas phase and that remaining in the solid particle.

220 Hence, an artificial interphase mass transfer term should be defined to account for the pore formation

221 rate. In the process of biomass fast pyrolysis, the pore formation rate depends on the rate at which

222 the biomass solid disappears because of the occurrence of heterogeneous reactions. This can be

223 affected by the particle shrinking rate as biomass decomposition causes not only pore-formation

224 inside a particle but also size change of the particle itself. Disappearance of the solid component in a

225 biomass particle is an overall result of decomposition reactions 2 and 3. This can be calculated from

226 the chemical kinetics, whilst calculation of the particle shrinking rate needs additional models. In this

227 work the 3-parameter shrinkage model proposed by Di Blasi [34] is used to account for the size change

228 of biomass particles during fast pyrolysis, described in detail in Section 2.4.

229 ## 2.3 Quadrature Method of Moment (QMOM) for Particle Population Balance Equation

230 (PBE)

231 Population distribution of a particulate system can be described generally with a particle number

232 density function with respect to different particle properties called the "internal coordinates", which

233 include particle size, shape and any other properties distinguishing the particles from one another. In

234 a fluidized bed, the number density is not only a function of these "internal coordinates", but also of

235 "external coordinates", including their spatial position and time. In order to integrate the particle

236 number density function to the current Eulerian multi-phase CFD framework, the conservation law for

237 a particle number with a specific property was applied to each control volume in the computational

238 domain. Since the only internal coordinate concerned in this study is the particle size, the PBE in an

239 Eulerian multi-phase flow framework can be written as in equation (3):

240
$$\frac{\partial n(L)}{\partial t} + \nabla \cdot \mathbf{u} n(L) = -\frac{\partial}{\partial L}\left[\frac{\partial L}{\partial t} n(L)\right]$$
(3)

241 Where, $n(L)$ is the number density function with respect to the particle size L. It can be seen clearly

242 that the above equation is a transient Eulerian equation with source terms. The term on the right hand

243 side of equation (3) denotes the source due to particle growth/shrinkage. In general, this equation

244 should include other source terms with respect to particle aggregation and fragmentation. Particle

245 aggregation hardly exists in a biomass fast pyrolysis fluidized bed; however, particle fragmentation

246 does occur. As far as we know, there have been no experimental methods developed to measure the

247 dynamics of particle fragmentation effectively and accurately in this kind of fluidized bed reactor.

248   Hence, only the particle shrinkage have been taken into account and other particle processes have

249   been ignored in this work.

250   Solving equation (3) directly would be extremely time-consuming due to its additional dimension of

251   particle size distribution. Randolph and Larson [60] proposed an indirect method for PBE time

252   evolution by calculating several low order moments of the number density function to reduce the

253   dimensionality and then solve a set of moment conservation equations. Nevertheless, a closure

254   equation set cannot be derived without knowing the particle size distribution. Where complex particle

255   phenomena are taken into account, such as size-dependent growth, particle fragmentation and

256   aggregation, this is especially the case. McGraw [61] approximated these moments with the n-point

257   Gaussian quadrature and finally improved the closure of this method for a broader range of particle

258   events. Xue and Fox [12] claimed that three integral quadrature abscissas can produce acceptable

259   simulation results for the particle size evolution in a biomass fast pyrolysis fluidized bed, which means

260   that only the first six, low order moment conservation equations need to be solved. Hence, the PBE

261   equation (3) is replaced by the following moment conservation equation in this study.

262
$$\frac{\partial \rho_s m_k}{\partial t} + \nabla \cdot \left(\rho_s \mathbf{u} m_k \right) = m_k \frac{\partial \rho_s}{\partial t} + \mathbf{u} m_k \cdot \nabla \rho_s - \rho_s \int_0^\infty k d_s^{k-1} \left[\frac{\partial d_s}{\partial t} n(d_s) \right] d(d_s) \quad k=0, \dots, 5 \quad (4)$$

263   Where, m_k denotes the moment of kth order; $n(d_s)$ is the number density function with respect to

264   particle diameter, which has the same meaning as $n(L)$ in equation (3). The zero order moment m_0

265   represents the total particle number density, the second order moment m_2 is related to total particle

266   area, and the third order moment m_3 relates to the total particle volume. However, based on the

267   definition of the moment, other low-order moments such as m_1, m_4 and m_5 have no clear physical

268   meanings.

269   ## 2.4 Di Blasi 3-parameter shrinkage model

270   Shrinkage of a biomass particle during the devolatilization process is very complex as it involves char

271   formation, structural change of the solid matrix, and pore formation. Di Blasi [34] studied the

272   shrinkage of the char layer formed in a wood slap pyrolysis subjected to a radiation heat flux. The total

273   volume of a biomass particle was considered to be a sum of the pore volume occupied by a gaseous

274   substance plus the solid volume remaining (volume occupied by char, unreacted biomass, and partly-

275   reacted biomass). Therefore, a shrinkage model with three shrinkage factors was proposed, with α, β,

276   γ representing different shrinkage contributions.

277   The volume occupied by the solid was assumed to decrease linearly with the biomass components

278   and to increase linearly with the char mass, as devolatilization takes place. The shrinkage factor α

279   reflects the density change of the solid residuals due to char formation, a value of α between 0 and 1

280   represents no density increase and maximum density increase, respectively.

281
$$\frac{V_S}{V_{W0}} = \frac{M_W}{M_{W0}} + \frac{\alpha M_C}{M_{W0}} \tag{5}$$

282   Where, V_s is the current solid volume; V_{w0} is the initial solid volume; M_W is the current mass of the

283   remaining biomass solid; M_{w0} is the initial mass of the biomass solid; M_c is the current char mass. The

284   volume occupied by volatiles is composed of two contributions, the first due to the initial volume of

285   pores, V_{g0}, and the second due to a fraction β of the volume left by the biomass solid as a consequence

286   of devolatilization, $V_{W0} - V_s$.

287
$$V_g = V_{g0} + \beta(V_{W0} - V_S) \tag{6}$$

288   The initial volume of volatiles in a biomass particle may also decrease with the size change of the

289   particle, depending on a reaction progress factor η, $\eta = M_W/M_{W0}$, and shrinkage factor γ.

290
$$V_{g0} = \eta V_{gi} + (1 - \eta)\gamma V_{gi} \tag{7}$$

291   Where, V_{gi} is the initial value of V_{g0} before the devolatilization process happens, depending totally on

292   the initial porosity of the biomass particle. The initial porosity of the biomass was assumed to be 0.5

293   in the current work [62].

294   2.5 Integration of the particle shrinkage into the CFD model

295   The key point of introducing the Di Blasi 3-parameter particle shrinkage model into the current CFD

296   framework is to translate the particle shrinkage pattern represented by different shrinkage factors

297   into the apparent density calculation and volume evolution occupied by volatiles inside the biomass

298   particle. The apparent density of the biomass particle is defined as the volume-weighted average of

299   the components' true densities according to equation (2). This can be considered further as the

300   volume-weighted average of the volatile (gaseous substances occupying the void) true density and the

301   solid (unreacted biomass and char) true density. The density of the volatile in pores is assumed to be

302   the same as that of the permanent gas in the gas phase, while the solid density depends on the value

303   of the shrinkage factor α in a specific shrinkage pattern. The volume-weighted mixing law is applied

304   to calculate the density of the remained solid substances and make it consistent with the value of α in

305   a specific shrinkage pattern by assigning a proper value to the char density.

306   In fact, differing β and γ values account for differing manners of volume evolution of the component

307   "void" in the biomass phase. By prescribing a set of these values, the mass transfer term between

308   "void" and permanent gas $m_{I^2,3^8}$ can be defined, and then the species transport equations are finally

309   closed. The shrinking rate of the biomass particle is the sum of the shrinking effects contributed from

310   "void" and solid. Equation (6) gives a simple expression that the total particle volume shrinkage rate

311   R (volumetric decreasing rate of the biomass phase per unit volume of the flow domain) is a sum of

312   those corresponding to void and solid volume change, respectively.

313
$$R = R_g + R_s \tag{8}$$

314   The volume occupied by the biomass phase in an Eulerian control volume can be calculated with

315     $V_b = \varepsilon_b V$, where V is the total volume of the control volume. The shrinking rate can then be written as

316   follows:

317
$$\frac{dV_b}{dt} = -RV \tag{9}$$

318   Let both sides of the above equation be divided by V_b:

$$\frac{1}{V_b}\frac{dV_b}{dt} = -\frac{RV}{V_b}$$ (10)

320   Substituting $V_b = N\pi d_b^3 / 6$ into equation (10) results into:

$$\frac{d(d_b)}{dt} = -\frac{Rd_b}{3\varepsilon_b}$$ (11)

322   Equation (11) gives the size-dependent particle shrinking rate, which is exactly the source term as it

323   appears in the moment conservation equations. Three different shrinkage patterns were investigated

324   in the current study, which were related to three sets of shrinkage factors, respectively (See Table 6).

325   Calculation of the volumetric shrinking rate, R, interphase mass transfer, $m_{1^2,3^8}$, and char density is

326   different, depending on the selected shrinkage pattern.

327   <div align="center">**Table 6 Different shrinkage patterns**</div>

No shrinkage: $\alpha=1$, $\beta=1$ and $\gamma=1$

$$\rho_{char} = \frac{1}{\alpha}\rho_b = \rho_b$$

$$m_{1^2,3^8} = \left[\rho_3\varepsilon_3(k_{2c}+k_{3c})x_{3,6} + \rho_3\varepsilon_3(k_{2h}+k_{3h})x_{3,7} + \rho_3\varepsilon_3(k_{2l}+k_{3l})x_{3,8}\right]\frac{\rho_{void}}{\rho_{biomass}}$$

$$-\left(\rho_3\varepsilon_3k_{3c}Y_c x_{3,6} + \rho_3\varepsilon_3k_{3h}Y_h x_{3,7} + \rho_3\varepsilon_3k_{3l}Y_l x_{3,8}\right)\frac{\rho_{void}}{\rho_{char}}$$

$$R_s = R_g = 0$$

Shrinkage pattern 1: $\alpha=1$, $\beta=0$ and $\gamma=1$

$$\rho_{char} = \frac{1}{\alpha}\rho_b = \rho_b$$

$$m_{1^2,3^8} = 0$$

$$R_g = 0$$

$$R_s = \left[\rho_3\varepsilon_3(k_{2c}+k_{3c})x_{3,6} + \rho_3\varepsilon_3(k_{2h}+k_{3h})x_{3,7} + \rho_3\varepsilon_3(k_{2l}+k_{3l})x_{3,8}\right]\frac{1}{\rho_{biomass}}$$

$$-\left(\rho_3\varepsilon_3k_{3c}Y_c x_{3,6} + \rho_3\varepsilon_3k_{3h}Y_h x_{3,7} + \rho_3\varepsilon_3k_{3l}Y_l x_{3,8}\right)\frac{1}{\rho_{char}}$$

Shrinkage pattern 2: $\alpha=0.5$, $\beta=0$ and $\gamma=0.5$

$$\rho_{char} = \frac{1}{\alpha}\rho_b = 2\rho_b$$

$$R_g = -m_{1^2,3^8} = 0.5\left[\rho_3\varepsilon_3(k_{2c}+k_{3c})x_{3,6} + \rho_3\varepsilon_3(k_{2h}+k_{3h})x_{3,7} + \rho_3\varepsilon_3(k_{2l}+k_{3l})x_{3,8}\right]\frac{\rho_{void}}{\rho_{biomass}}$$

$$R_s = \left[\rho_3 \varepsilon_3 (k_{2c} + k_{3c}) x_{3,6} + \rho_3 \varepsilon_3 (k_{2h} + k_{3h}) x_{3,7} + \rho_3 \varepsilon_3 (k_{2l} + k_{3l}) x_{3,8} \right] \frac{1}{\rho_{biomass}}$$

$$- \left(\rho_3 \varepsilon_3 k_{3c} Y_c x_{3,6} + \rho_3 \varepsilon_3 k_{3h} Y_h x_{3,7} + \rho_3 \varepsilon_3 k_{3l} Y_l x_{3,8} \right) \frac{1}{\rho_{char}}$$

328

329 In the case of the no shrinkage pattern, each shrinkage factor takes the value of unity. An artificial

330 mass transfer from the permanent gas to the "void" is required to compensate for the volume loss

331 due to biomass decomposition so that the particle size can remain constant. In the case of shrinkage

332 pattern 1, shrinkage factor β comes to 0, and the other two factors stay the same as the above case.

333 This means that the "void" volume depends on the initial volume only, i.e. no artificial mass transfer

334 is needed. Particle size change, in this case, is attributed wholly to the net volume loss of the solid

335 substance. In the case of shrinkage pattern 2, the initial volume of the volatile varies with the reaction

336 progress. It is assumed that 50% of the initial volatiles leave the biomass particle as a consequence of

337 particle size decrease. So, an artificial mass transfer from the "void" to permanent gas needs to be

338 defined to account for this gaseous volume loss. It should be noted that, though the artificial mass

339 transfers introduced in the case of no shrinkage pattern and shrinkage pattern 2 are both between

340 permanent gas and the "void", the mass transfer directions are the opposite.

341 ## 3. Model setups and solution strategy

342 ### 3.1 Model geometry and solution strategy

343 The geometrical model of the simulation in this study is based on a 300g/h lab-scale cylinder fluidized

344 bed reactor for biomass fast pyrolysis. Simulation was carried out using a 40mm×340mm 2-D

345 computational domain, shown in Figure 2, and considering a height of the pre-loaded sand of 80mm.
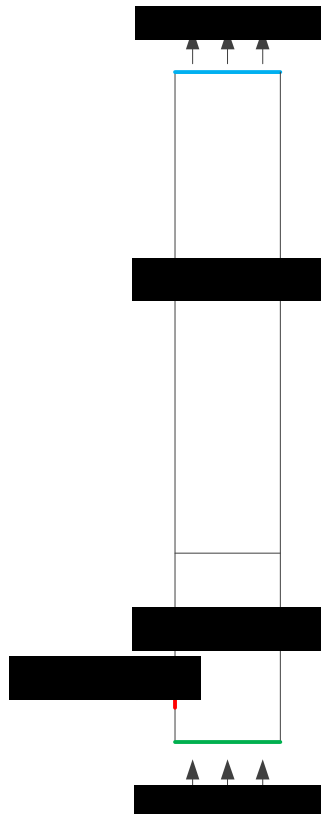
Fig. 2 The 2-D computational domain of the fluidized bed for numerical simulation

The phase-coupled SIMPLE algorithm was employed for pressure-velocity coupling. A volume of fraction (VOF) equation was obtained for each solid phase from the total mass continuity. An explicit variable arrangement was used for the VOF equation. Updating of the VOF at each iteration, was included to achieve timely and better convergence, with a guarantee that the volume fraction of each biomass phase matched the density updating. The volume fraction of the gas phase is obtained directly from the law of unity. A second order upwind scheme was generally used in accounting for the convection term discretization in the flow equation, energy equation, and species transport equations. The three order upwind-like QUICK scheme was used for the VOF equations in order to obtain high VOF precisions for each secondary phase. For temporal discretization, the first order implicit method was employed. A relatively small time step length of 5×10^{-5}s was used at the beginning of the simulation to overcome the difficulty of convergence due to poor initial fields, and a fixed time step length of 2×10^{-4}s was used afterwards when simulation became stable.

360 ## 3.2 Initial and boundary conditions

361 The biomass particles were assumed to be perfect spheres with a Sauter mean diameter of 325μm,

362 following a normal distribution for the particle size. Based on this size distribution, the low order

363 moments of the biomass feedstock were calculated, providing the boundary condition of the PBE at

364 the biomass inlet. Table 7 gives the 0th-5th order moments of the size distribution.

365 **Table 7 Low order moments of the feed stock**

Moments	Calculation method
Moment-0	$m_0 = N$
Moment-1	$m_1 = \bar{d}m_0$
Moment-2	$m_2 = 2\bar{d}m_1 - \bar{d}^2 m_0 + \sigma^2 N^2$
Moment-3	$m_3 = 3\bar{d}m_2 - 3\bar{d}^2 m_1 + \bar{d}^3 m_0$
Moment-4	$m_4 = 4\bar{d}m_3 - 6\bar{d}^2 m_2 + 4\bar{d}^3 m_1 - \bar{d}^4 m_0 + 3\sigma^4 N^4$
Moment-5	$m_5 = \bar{d}m_4 - 10\bar{d}^2 m_3 + 10\bar{d}^3 m_2 - 5\bar{d}^4 m_1 + \bar{d}^5 m_0$

366 Where, N denotes the total particle number per unit volume of the feed stock; $\sigma = 0.3\bar{d}$; and $\bar{d}$ is the

367 number-mean diameter. Table 8 gives the specific values of these moments as well as other model

368 parameters.

369 **Table 8 Model parameters and simulations conditions**

Parameters	Value
Biomass feeding rate (g/h)	180 (Equivalent to a cylinder experimental rig)
Nitrogen inflow velocity (m/s)	0.3
Minimum fluidized velocity (m/s)	0.081
Biomass feeding temperature (K)	300
Nitrogen feeding temperature (K)	773
Wall temperature (K)	773
Gas density (kg/m³)	Incompressible ideal gas law
Gas viscosity (Pa·s)	3.507×10^{-5} (773K)
Biomass particle size (μm)	325 (Sauter mean)
Initial moments of the biomass particle	
Moment0	6.924×10^{10}
Moment1	1.932×10^7
Moment2	5875
Moment3	1.910
Moment4	6.563×10^{-4}
Moment5	2.366×10^{-7}
Biomass component true density (kg/m³)	
Cellulose, hemicellulose, lignin	800
Char density for no shrinkage	800
Char density for shrink pattern 1	800
Char density for shrink pattern 2	1600
void	Same as gas

Biomass component initial mass fraction	
Cellulose	4.094×10^{-1}
Hemicellulose	3.195×10^{-1}
Lignin	2.696×10^{-1}
void	1.529×10^{-3}
Biomass initial porosity (m^3 gas/ m^3 particle)	0.5
Biomass initial apparent density (kg/m^3)	400
Sand particle size (μm)	440
Sand density (kg/m^3)	2500
Sand initial packing height (mm)	80
Sand initial packing limit	0.63

370

371 3.3 Implementation of the simulation

372 In order to implement the simulation of the mathematical model depicted above, two additional

373 assumptions should be made. First, an even temperature distribution inside the biomass particle is

374 always achieved throughout the simulation; which means internal heat resistance is ignored. The

375 assumption is safe because of the low Bi number of the particle itself. Second, volatiles produced due

376 to the devolatization process are released instantaneously into the gas phase; which means

377 heterogeneous reactions play a dominant part in the interphase mass transfer process instead of

378 diffusion. This assumption is also safe because of the fairly small size of the biomass particle used in

379 this study.

380 The mathematical model of the fluidized bed was simulated with a widely used CFD package FLUENT

381 16.2. The interphase mass transfer between "void" and permanent gas, heat transfer between the

382 biomass phase and the bed medium, and source terms of the moment conservation equation due to

383 particle density and size variation, were accounted for by proper DEFINE MACROs of the FLUENT UDF

384 system. Each case in this study was run in parallel on an HPC cluster with 80 computing nodes, each

385 of which has two Intel E5-2660 CPUs, giving 16 CPU cores. Results gained from the simulation are

386 discussed in detail in the following sections.

4. Results and discussion

4.1 Operational steady state of the fluidized bed

Since a mathematically rigorous steady state, in which all the field variables remain constants cannot be reached in a fluidized bed, a transient solver is employed to carry out this kind of simulation. The fluidized bed reactor reaches an operational steady state when the main field parameters reach fixed values statistically at a specific time after the start-up. Not all of the field variables reach steady state simultaneously for a single simulation process. Within this study, the hydrodynamics of the fluidized bed seemed less sensitive to the initial field and achieved a steady state after a few seconds from the beginning of the simulation. Typically, the biomass hold-up of the fluidized bed increased rapidly in the first 5 seconds due to injection and reached an approximate constant value after 20 seconds, when a steady output of the solid residue was set up. In contrast, the thermal steady state depends largely on the initial temperature field. Xue *et al.* [21] observed that more than 100 seconds were required to reach a thermal steady state when the initial temperature field deviated significantly from the final temperature field, whereas if an appropriate initial temperature field is adopted, a thermal steady state can be achieved in a few seconds. In this work, an initial temperature of 773K was used throughout the fluidized bed to guarantee a rapid achievement of the thermal steady state.

4.2 Grid dependency test

According to Min *et al.* [63], numerical simulations with a <4mm mesh can produce predictive results of the main characteristics of a lab-scale fluidized bed. At the beginning of this work, a grid dependency test were carried out with grid resolutions of 4mm, 2mm and 1mm. Results of some most interested parameters of this study such as particle apparent density, particle diameter are plotted against vertical axis of the fluidized bed reactor in Figure 3. Our test shows that all of the three grid resolutions give very close results, especially for outlet values, and can be referred approximately as grid-independent solutions. Additionally, the 1mm and the 2mm grids seem to give better predictions than the 4mm grid across the splashing zone of the fluidized bed, especially for particle size evolution, see

412   Figure 3 (b). In balancing computational accuracy and efficiency, a uniform 2mm×2mm mesh was

413   finally adopted in this study.

414
415   (a)
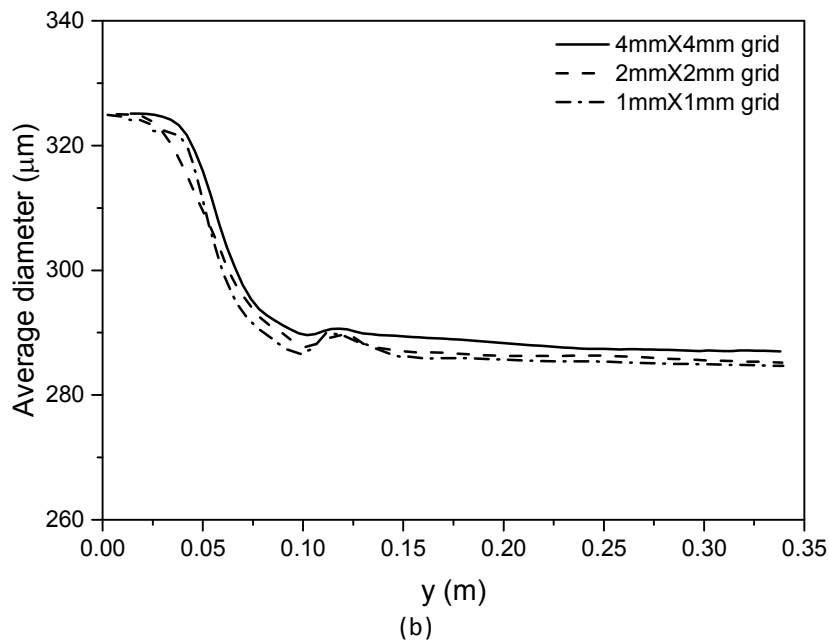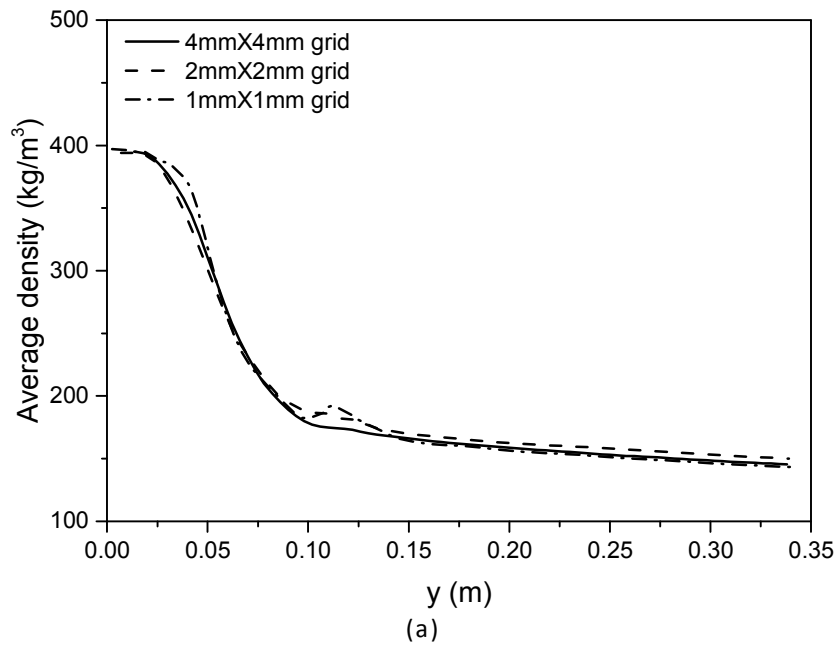
416
417   (b)
418   **Fig. 3 Grid dependency test: (a) average density and (b) average particle size of the biomass**
419   **phase variation along the y axis at steady state (shrinkage pattern 1)**

420

421   4.3 Density and size evolution of the biomass particles

422   Figure 4 (a) exhibits snapshots of the gas volume fraction distribution of the fluidized bed reactor

423   corresponding to 0.05s at steady state around 24s and the particle shrinkage pattern 1. Results show

424   typical bubble formation, growth, rise, and breakage within the fluidized bed reactor. Solid particles

425   are firstly lifted up by the rising bubbles and then fall down due to density difference. These chaotic

426   motions of gas and solid particles largely enhance phase mixing, and heat and mass transfers. Cold

427   biomass particles are injected into the reactor and mix rapidly with the hot bed medium. As a result,

428   the volume fraction decreases by almost two orders of magnitude compared to the feeding state. This

429   occurrence can be observed in Figure 4 (b), which shows a snapshot of biomass volume fraction

430   distribution at 24s in the case of particle shrinkage pattern 1. The biomass phase cannot fill the whole

431   dense zone before entering the free board due to short particle residence time, which explains the

432   high concentration region adjacent to the feeding port. Because of the endothermic nature of the

433   decomposition reaction and low temperature of the feedstock (300K), an apparent temperature

434   gradient arises near the high concentration zone for the biomass phase (see Figure 5 (a)).

435   Devolatilization occurs inside the biomass particle when a certain temperature is reached. Pores are

436   formed as a consequence of continuous mass loss due to volatile release, which may result in a drop

437   in apparent density of the biomass particle. On the other hand, apparent density may increase due to

438   the increase in true densities of the solid components according to Di Blasi's shrinkage theory, in which

439   the shrinkage factor α accounts mostly for true density variation of the solid with respect to solid

440   matrix reconstitution happening during the char formation process.
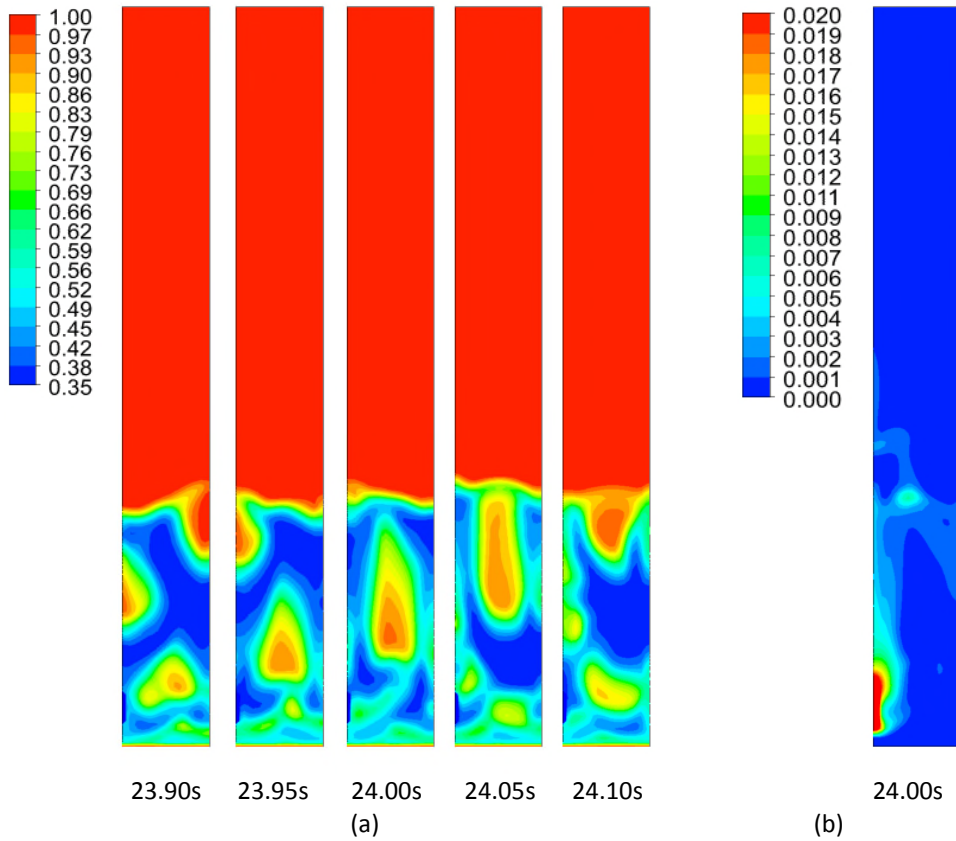
441
442   23.90s   23.95s   24.00s   24.05s   24.10s   24.00s
443   (a)   (b)
444   **Fig. 4 Snapshots of volume fraction distribution at steady state, shrinkage pattern 1: (a)**
445   **Gas phase; (b) biomass phase**
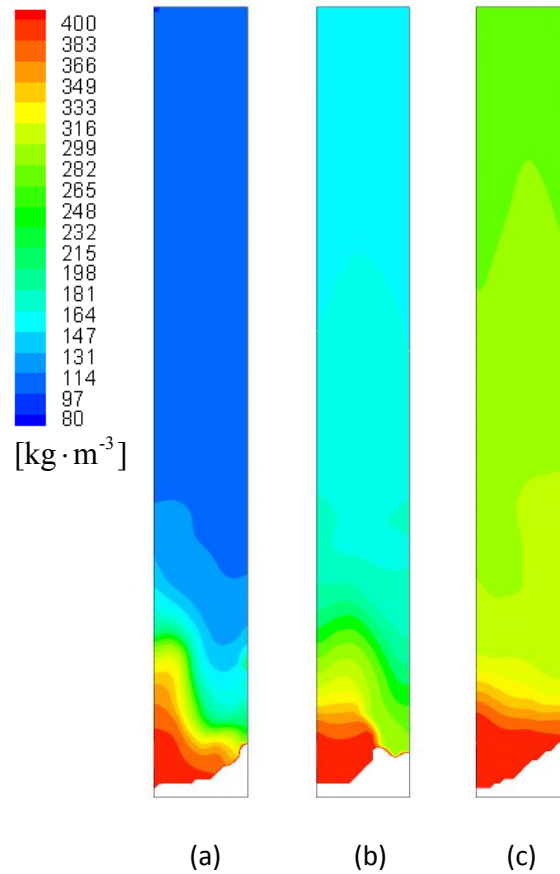

                         [K] $[kmol \cdot m^{-3} \cdot s^{-1}]$

446
447   (a) Temperature   (b) Decomposition rate
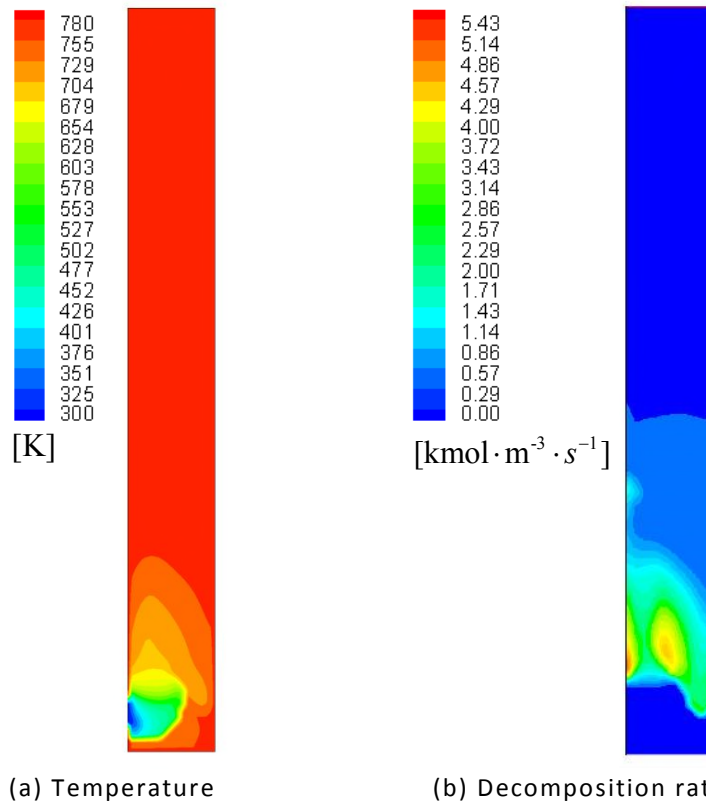
448   **Fig. 5 (a) Distribution of temperature and (b) decomposition rate of the biomass phase in**
449   **the fluidized bed at 24s (data derived from shrinking pattern 1)**

450   The apparent density distribution of the biomass phase in a fluidized bed is an overall result of particle

451   motion, heat transfer and heterogeneous reactions. Figure 6 shows the apparent density distribution

452   for biomass particles with different shrinking patterns at 24s. It can be observed that the particle

453   apparent density decreases throughout the vertical axis of the fluidized bed reactor in all of the three

454   shrinkage patterns. A sharp density gradient is observed close to the biomass injection point in the

455   dense zone of the fluidized bed. This is where devolatilization reactions occur intensively, see Figure

456   5 (b) – an example of reaction rate distribution at steady state. It is clear that the biomass particles

457   are heated rapidly in the dense zone and begin to reach the pyrolysis temperature at around 500K a

458   short distance away from the injection point. In the free board of the fluidized bed, the density

459   gradient of the biomass particle is much lower as most of the devolatilization reactions are finished in

460   the dense zone. In addition, the apparent density profile is different depending on the shrinkage

461   pattern. In the case of no shrinkage, the apparent density drops from 400 kg/m^3 at the inlet of the

462   reactor to 95 kg/m^3 at the outlet. In the case of shrinkage patterns 1 and 2, the values at the outlet

463   are 160 kg/m^3 and 245 kg/m^3, respectively. Obviously, the highest level of apparent density decrease

464   appears in the case of no shrinkage pattern, then shrinkage pattern 1 and finally shrinkage pattern 2.

465   This is because biomass decomposition in the case of no shrinkage leads wholly to pore formation,

466   while in the other two cases particle size decrease is also the result of the biomass decomposition.

467   The apparent density of the biomass particle could actually increase and exceed the initial value of

468   400 kg/m^3, if smaller values of α and γ were used (for example α=0.2, γ=0.2). This is because smaller

469   values of α and γ represent a larger degree of solid matrix reconstitution during the char formation

470   process and lesser degree of pore formation respectively, which is equivalent to a dominant

471   reconstitution of the solid matrix during the process of biomass pyrolysis. These results are not shown
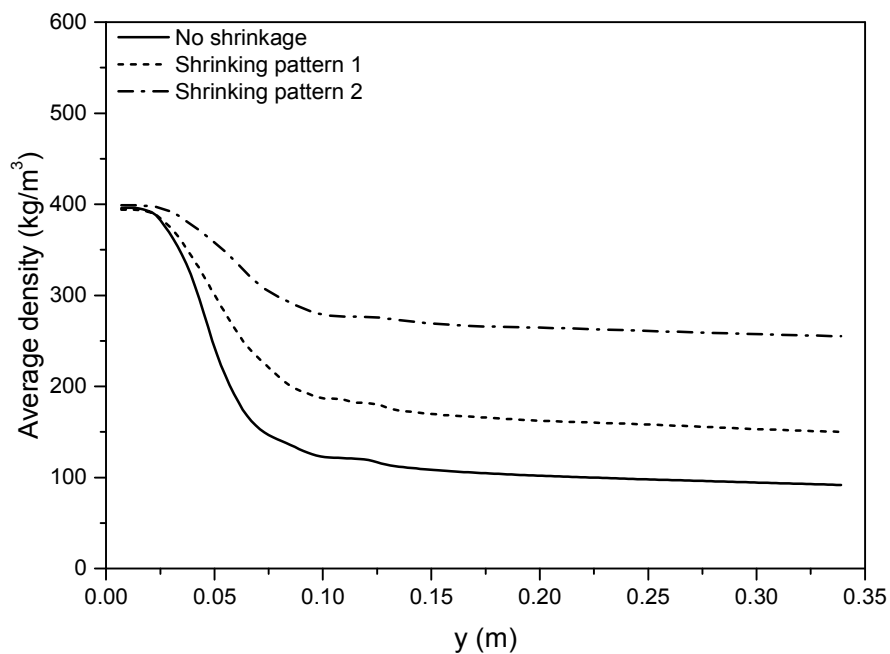
472   here.

473
$$\overline{\rho}_{apparent,y} = \frac{\iint_{t\ x} \varepsilon_{x,y} \rho_{apparent,y} dVdt}{(t_2 - t_1) \int \varepsilon_{x,y} dV} \tag{12}$$

400
383
366
349
333
316
299
282
265
248
232
215
198
181
164
147
131
114
97
80

$[\text{kg}\cdot\text{m}^{-3}]$

474
475   (a)   (b)   (c)
476   **Fig. 6 Apparent density distribution of the biomass particles inside the fluidized bed at 24s:**
477   **(a) no shrinkage pattern; (b) shrinkage pattern 1; (c) shrinkage pattern 2**


478
479   **Fig. 7 Spatial-temporal averaged density of the biomass particles in different shrinkage**
480   **patterns along the y axis**

481   Figure 7 gives a statistical average result of the biomass density variation in the fluidized bed reactor

482   in terms of spatial-temporal averaged value along the y axis. The diagram was developed by calculating

483   the volume-fraction-weighted mean density at each cross section of the fluidized bed and averaging

484   it over a period of time after steady state was finally achieved (see equation 12). Oscillations of the

485   stochastic instantaneous results were smoothed. These results give the apparent density evolution of

486   the biomass particles quantitatively in the fluidized bed and in good agreement with the phenomena

487   exhibited in Figure 6.

488   Particle size evolution for different shrinking patterns is illustrated in Figure 8. 0th-5th moment

489   conservation equations of the biomass phase were solved together with all other transport equations

490   synchronously; and the Sauter mean diameter of the biomass phase was derived from m_3/m_2 for every

491   control volume in the computational domain. As expected, particle size remained constant and equal

492   to the initial value at any point within the domain in the case of no shrinking pattern. In the case of

493   shrinking patterns 1 and 2, the particle size decreased related to the progress of the biomass

494   decomposition. Similarly to the apparent density, the highest gradient of particle shrinkage was

495   observed near the inlet area where the devolatilization and heterogeneous reactions mainly occur. It

496   was also observed that the temperature profile of the biomass phase was insensitive to different

497   shrinkage patterns in the current study. Figure 9 gives the spatial-temporal averaged temperatures of

498   the biomass phase along the y axis of the fluidized bed. It can be seen that curves representing

499   different shrinkage patterns overlap with each other in most parts of the reactor. Figure 10 gives the

500   spatial-temporal-averaged value of the biomass particle diameter along the y axis of the fluidized bed.

501   Simulation results show that the average diameter of the biomass particle drops to 290μm and 250μm

502   near the outlet of the fluidized bed for shrinking patterns 1 and 2, respectively. The pattern in which

503   a biomass particle shrinks not only depends on the physical properties of the particle itself, such as

504   size, shape, composition, structure, etc., but also on the surrounding heat and mass transfer

505   environment. Like some researchers in their work [28, 34], the shrinkage factors investigated in the

506   current study were given arbitrarily. To our knowledge, no current work gives an exact correlation

507   between the shrinkage factor and a specific type of biomass particle. Therefore, this work focuses

508 more on demonstrating a method to consider the particle shrinkage in a CFD simulation instead of

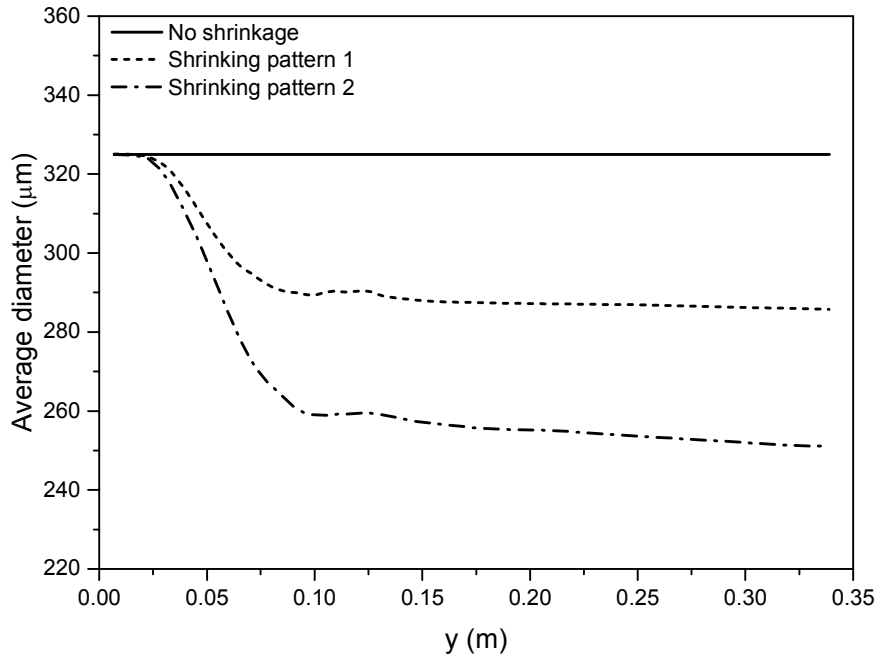509 predicting an exact result for a real process.
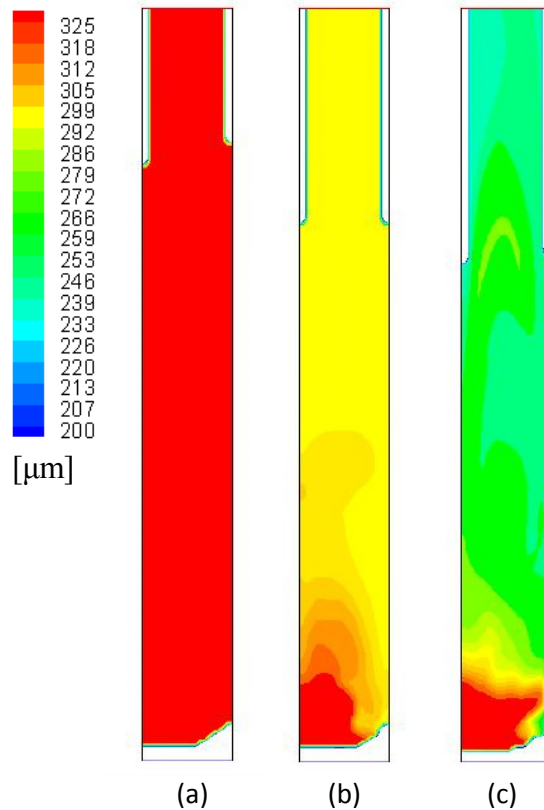
510
511   (a)   (b)   (c)
512 **Fig. 8 Size distribution of the biomass particles inside the fluidized bed at 24s: (a) no**
513   **shrinkage pattern; (b) shrinkage pattern 1; (c) shrinkage pattern 2**
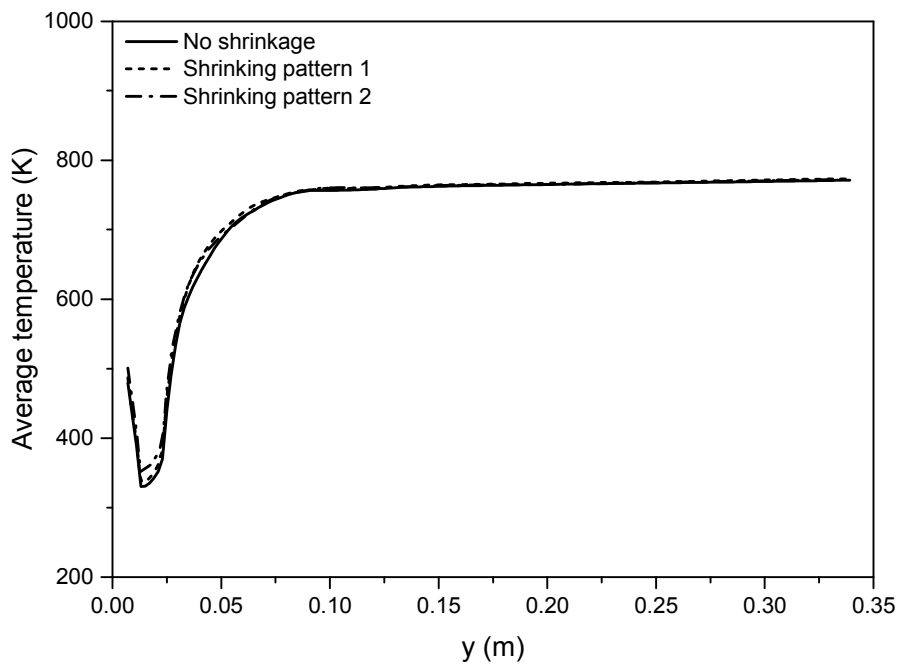
514
515 **Fig.9 Spatial-temporal averaged temperature of the biomass particles in different shrinkage**
516   **patterns along the y axis**

Fig. 10 Spatial-time averaged diameter of the biomass particles in different shrinkage patterns along the y axis

4.4 Particle tracking in an Eulerian CFD framework

Knowledge of particle motion is of great importance for the design of fluidized bed reactors, since it can help to optimize the reactor configuration and choose reasonable operating conditions. In general, two methods are used to simulate particle laden flows in a fluidized bed reactor, the Eulerian-granular model and the Discrete Element Method DEM-CFD model. The latter is more suitable for particle trajectory calculation as the complex fluid-particle and particle-particle interactions are investigated by tracking a great number of 'real' particles individually; however, this method is extremely computational expensive. In contrast, the computing cost of the Eulerian-granular method is much lower because the particles are considered as a continuum, and particle-particle and particle-fluid interactions are accounted for by means of solid viscosity closured by the granular kinetic theory and drag force models, respectively. Particle tracking is also possible under the Eulerian-granular framework, which is referred as the 'fictitious tracer particle' concept proposed by Liu and Chen [64]. The concept of massless particle, routinely used by many researchers [65-67], is based on the calculation of the trajectory of a moving Lagrangian element with the knowledge of an Eulerian flow

535   field. The tracer velocity can be either assigned by the local velocity of the nearest cell or extracted

536   with high-order numerical schemes [68-70]. Each fictitious tracer particle can be laid in an interested

537   computational cell at a specific physical simulation time and fully follow the movement of the solid

538   phase. The tracer particle is massless and the velocity is assigned by the solid phase velocity of the cell

539   where the tracer particle is located. Thus, the displacement of the tracer particle can be calculated

540   after a time interval, and a new position of the particle is then obtained. When this procedure is

541   repeated within each time step during the simulation, the trajectory of each tracer particle is obtained.

542   Although this is not a rigorous particle tracking technology based on 'real' particles, some important

543   particle motion information can be obtained. Forces exerted on the tracer particle, such as fiction and

544   collision, are implied in the solid phase motion accounted for by the kinetic theory.

5.00E-02	
3.61E-02	
2.60E-02	
1.87E-02	
1.35E-02	
9.74E-03	
7.03E-03	
5.07E-03	
3.65E-03	
2.63E-03	
1.90E-03	
1.37E-03	
9.87E-04	
7.12E-04	
5.13E-04	
3.70E-04	
2.67E-04	
1.92E-04	
1.39E-04	
1.00E-04	

                              (a)   (b)
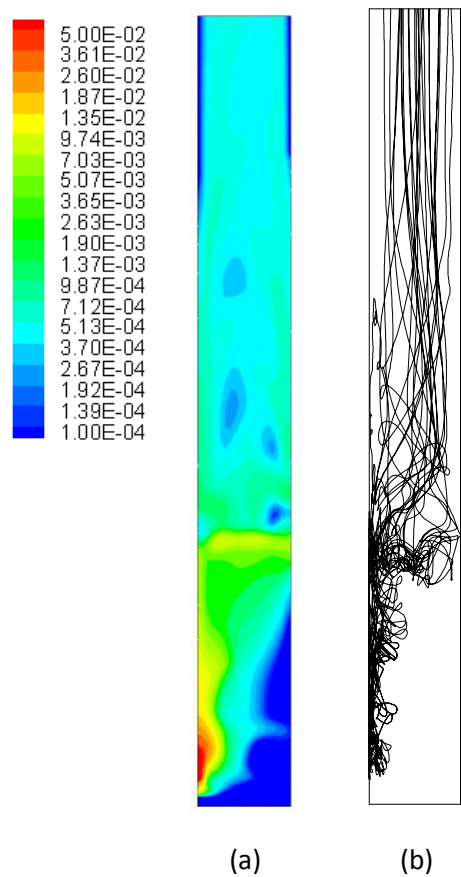
545
546
547
548   **Fig. 11 (a) The biomass volume fraction and (b) comparison of the particle trajectories in**
549   **the fluidized bed at 24s (no shrinkage pattern)**
550   Solid and vapour residence time are also parameters of great importance for a biomass pyrolysis

551   fluidized bed. These variables are closely related to parameters such as biomass conversion, char

552   distribution, secondary reaction occurrence, etc. Vapour residence time can be estimated by means

553   of the superficial velocity of the fluidized gas and the gas phase effective volume in the fluidized bed.

554   However, solid residence time cannot be estimated in this way, since particles shrink and flow back

555   far more frequently than in the gaseous phase. In order to estimate the solid residence time of the

556   fluidized bed, 'fictitious tracer particle' concept was applied in this work. Massless tracer particles

557   were released one by one at different positions near the biomass inlet for every 50 time steps and

558   tracked in accordance with the transient update of the flow field. The velocity of an individual tracer

559   particle is assigned by the local velocity of the biomass phase at the control volume where the particle

560   is currently located. If the tracer particle moves and touches the walls, a full elastic reflection happens

561   so that a continuous particle trajectory can be obtained until the particle leaves the domain from the

562   top outlet. Most of the particles leave the domain after a certain period of tracking. However, a few

563   may be trapped permanently because zero-velocity regions exist at the two sides close to the outlet

564   of the fluidized bed. In addition to residence time, other particle information can be recorded

565   dynamically with this tracking technology. Any of the parameters of interest can be stored in a data

566   matrix when implementing the tracking process, similarly to that of storing the position information,

567   such as particle temperature, local sand volume fraction, etc. Some statistically averaged

568   characteristics of the biomass phase behaviour can be obtained by tracking a large number of

569   individual particles in a fluidized bed. Figure 11 gives a comparison of biomass volume fractions

570   alongside a number of particle trajectories. It can be observed that regions with dense particle

571   trajectories correspond accordingly with high volume fractions derived from the VOF equation.

572   Particles entering the domain with a low initial velocity from the inlet are unlikely to spread

573   immediately across a wide range within the fluidized bed medium. Instead, most of them travel along

574   the side wall to the top of the dense zone until reaching the splashing zone where more intensive

575   mixing happens due to bubble breakage; hence particles spread faster throughout the whole splashing

576   zone.

(a)   (b)   (c)
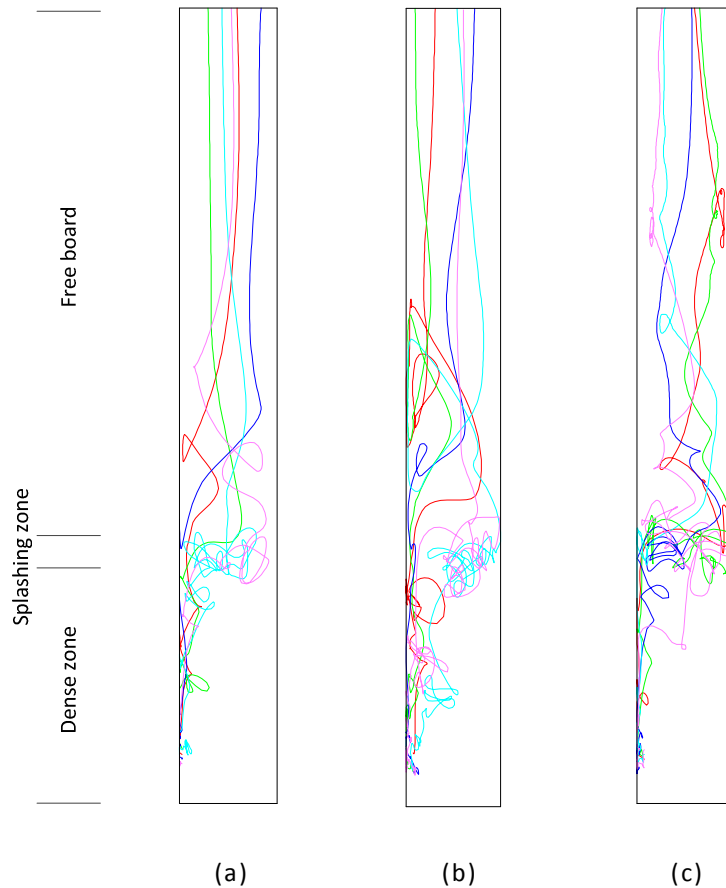
Fig. 12 Typical particle trajectories of the biomass particle in different shrinking pattern: (a) no shrinkage pattern; (b) shrinkage pattern 1; (c) shrinkage pattern 2

Differences in the biomass particle motion inside the fluidized bed due to the implementation of a

different particle shrinkage pattern can be observed by means of the trajectories of the particles.

Figure 12 shows typical particle trajectories for different shrinkage patterns. It can be seen that, when

no shrinkage pattern is considered, most of the particles are likely to escape the splashing zone into

the free board without significant flow back (such as the red, blue and green lines in Figure 12(a)).

Nevertheless, some of the particles cannot directly escape the splashing zone and stay for some time

before entering the free board area (cyan and purple lines in Figure 12(a)). In the case of shrinkage

pattern 1, the flow back of the particles in the splashing zone and the area immediately after this zone

is more frequent. This may be related to the higher particle density which seems then to have a higher

influence on the particle motion than that of the particle size. In the case of particle shrinkage pattern

2, few particles escape the splashing zone directly. Most are trapped in the splashing zone for different

periods of time before entering the free board. Particles undergoing shrinkage pattern 2 flow back

593   frequently, even once they are in the free board area and near to the outlet of the reactor (see Figure

594   12(c)).

595   Figure 13 shows the spatial-temporal-average y-velocity of the biomass particles inside the fluidized

596   bed. In the case of no shrinkage pattern and shrinkage pattern 1, the y-velocity of the biomass phase

597   is positive, on average, across the splashing zone, which means that back flow is not dominant. In the

598   free board, the velocity observed when no shrinkage is implemented is slightly higher than that of

599   shrinkage pattern 1, leading to a slightly shorter residence time. In contrast, in the case of shrinkage

600   pattern 2, the average y-velocity is negative across the splashing zone which shows significant back

601   flow and longer residence time of the particles in this area.

602   Figure 14 (a) gives a comparison of the biomass particle residence time in the dense zone. This was

603   obtained by recording the time when the volume fraction of the sand phase becomes zero during the

604   particle tracking process. Over 200 particles were tracked for each shrinkage pattern to obtain

605   statistically average values for the residence time. Bar diagrams were drawn by counting the number

606   of particles for specific time intervals. As can be observed, in the case of the no shrinkage pattern, a

607   major peak appears at around 1.8s on the curve of the number density distribution. The majority of

608   particles (71%) in this case leave the dense zone in up to 2.8s. This peak occurs slightly later in the case

609   of shrinkage pattern 1, at about 2.4s. In addition, a second obvious peak arises around 3.6s. This

610   situation can be attributed to the non-negligible number of particles trapped when passing through

611   the splashing zone. Therefore, the residence time in this case increases up to 3.6s for about 74% of

612   the total particles tracked. In the case of shrinkage pattern 2, this proves to be much more common

613   as most of the biomass particles are trapped in the splashing zone and eventually escape only by

614   chance. Hence, more than one peak appears, and the whole probability density profile distributes

615   more evenly than the other two shrinkage patterns. As a result, particle residence time increases more

616   in this case, and 73% of the tracer particles leave the dense zone in 4.7s.

617   The total residence time of the biomass particles in the whole domain can be similarly estimated by

618   recording the time when a particle approaches the outlet of the reactor. Figure 14 (b) gives the

619   probability density distribution of the total particle residence time for this domain. For the no

620   shrinkage pattern, a major peak appears around 2.9s, followed by two other small peaks around 4.8s

621   and 5.6s, respectively. For shrinkage pattern 1, two peaks of similar size appear at about 3.2s and 4.4s,

622   respectively. For shrinkage pattern 2, five obvious peaks appear at 4s, 4.8s, 5.6s, 9.2s and 10.8s,

623   representing different particle escape modes from the splashing zone.
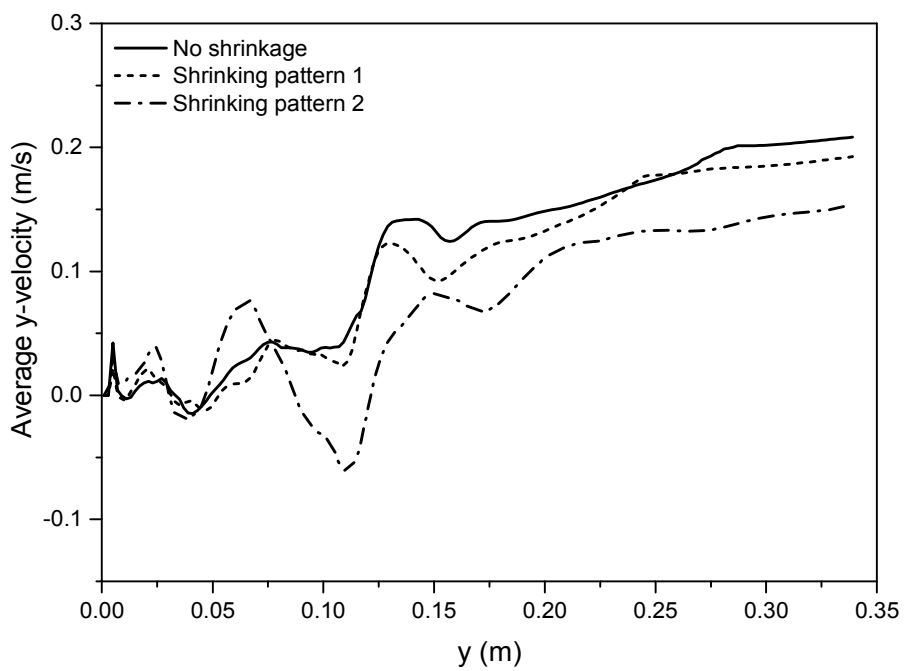
624

625   **Fig. 13 Spatial-temporal averaged y-velocity of the biomass particles with different**
626   **shrinking patterns along the y axis**

627

628

(a)

629

630

(b)
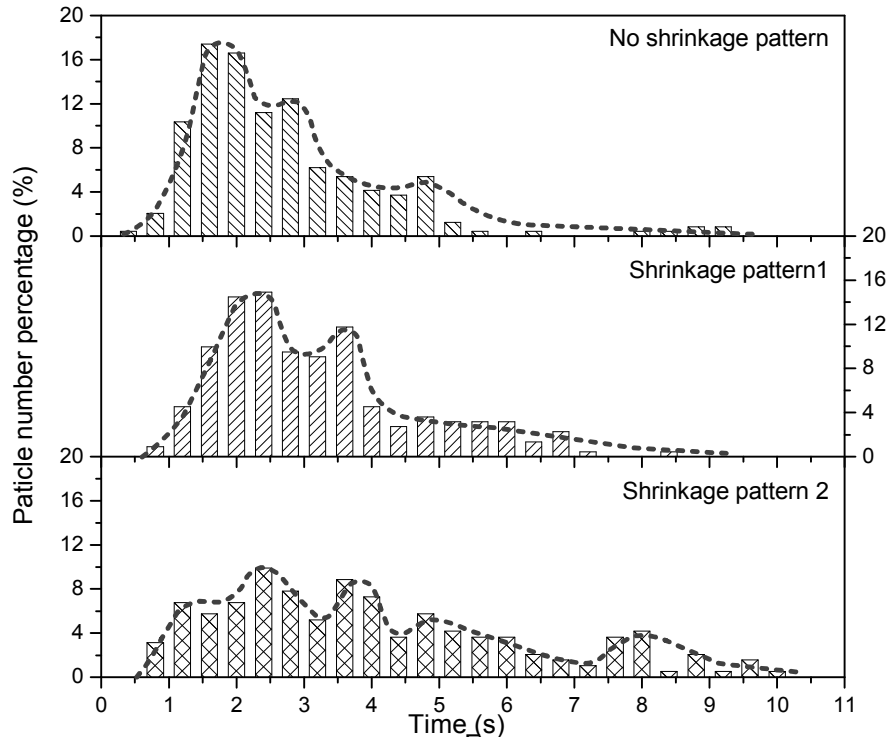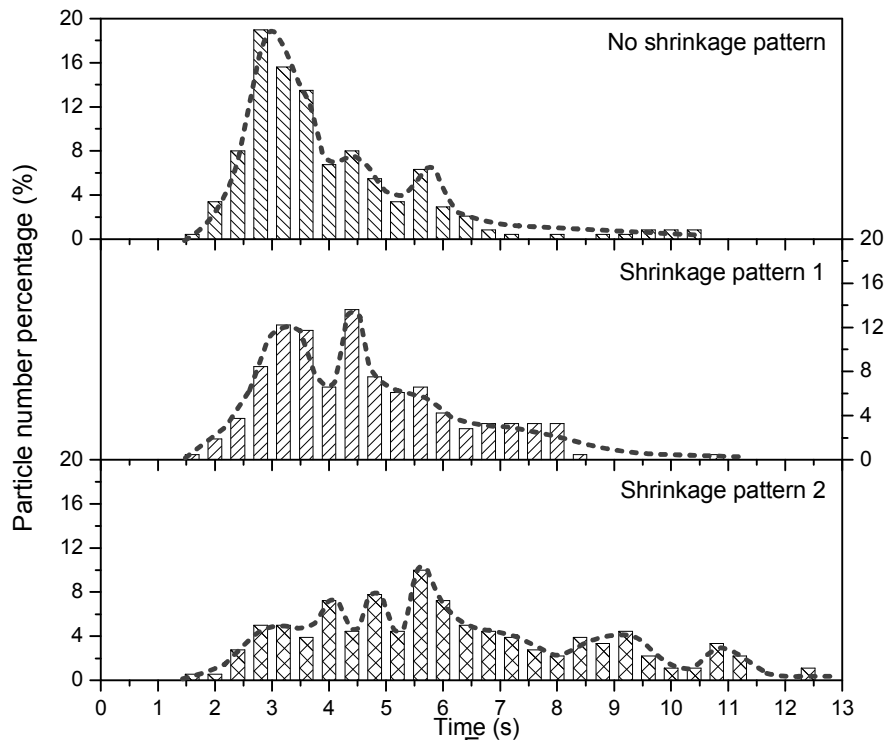
631   **Fig. 14 Residence time of the biomass particles in (a) the dense zone and (b) the whole**

632   **domain**

633 It should be pointed out that these characteristic time values are rough estimations as the total

634 number of the tracer particles are limited. Moreover, in the case of shrinkage pattern 2, about 10% of

635 the tracer particles were still trapped in the splashing zone when tracking terminated, due to the pre-

636 set maximum tracking time limit being reached. Based on these particle tracking data, the number-

637 weighted-average residence time was calculated and is shown in Table 9. This provides an outline of

638 the effects of shrinkage patterns on particle residence times.

639

Table 9 Particle average residence time

Shrinkage pattern	Residence time (dense zone(s))	Residence time (domain(s))
No shrinkage	2.69	3.96
Pattern 1	3.17	4.60
Pattern 2	4.04	5.73

640

641 ## 4.5 Product yields of different shrinkage patterns

642 Results for product yields were compared to results obtained from experiments carried out in reactors

643 with similar geometry, feedstock composition (cellulose: 32-52%; hemicellulose: 23-33%; lignin: 13-

644 27%) and operating conditions to those used in this work [22, 71]. The simulation results for the

645 different particle shrinkage patterns and experimental results are compared in Table 10. The product

646 yields from the model are calculated as an average of each of the species flow rate at the outlet of the

647 fluidized bed. In general, simulation results are in good agreement with the experimental results,

648 especially those obtained by Patel [71]. It can be observed that the bio-oil yield seems insensitive to

649 particle shrinkage patterns, which is approximately 63%. However, significant changes in non-

650 condensable gas and char yields are observed depending on the shrinkage pattern applied (i.e. 1 or 2).

651 Indeed, the application of shrinkage pattern 2 gave rise to higher biomass conversion and char yield

652 than that obtained with pattern 1 and with no shrinkage pattern. This might be attributed to the longer

653 residence time of the biomass particle, which has been discussed in section 4.4. From the three main

654 constituents of the biomass, hemicellulose has the most reaction activity, then cellulose; lignin has

655   the lowest reaction activity, which in turn contributes the most to non-reactive residues. The increase

656   in the residence time of the biomass particle in the fluidized bed may allow increasing the conversion

657   of lignin, which is known to lead to higher char yields [72].

658   **Table 10 Product yields (experiments from literature and simulation result at different shrinkage patterns)**

Method	Feed stock	Bio-oil yield (wt. %)	Non-condensable gas yield (wt. %)	Char yield (wt. %)	Residue (wt. %)	Temperature (K)	Particle size (mm)
Experiment [a]	Beech wood	63.87	11.69	14.83		779-798	0.25-1.0
Experiment [b]	Bagasse pallet	60.45	14.01	17.32		779-798	0.25-1.0
Experiment [c]	Red oak	71.7 ± 1.4	20.5 ± 1.3	13.0 ± 1.5	-	773	0.25-0.4
Simulation no shrinkage	-	62.83	11.18	14.93	10.76	771.45 [d]	0.325 [e]
Simulation shrinkage 1	-	63.40	10.49	15.50	10.47	773.56 [d]	0.325 [e]
Simulation shrinkage 2	-	63.38	12.18	17.83	6.51	772.46 [d]	0.325 [e]

659   Note: a, b - experimental data from Patel, 2013; c - experimental data from Xue *et al.*, 2012; d - outlet temperature

660   e - Sauter mean diameter

661
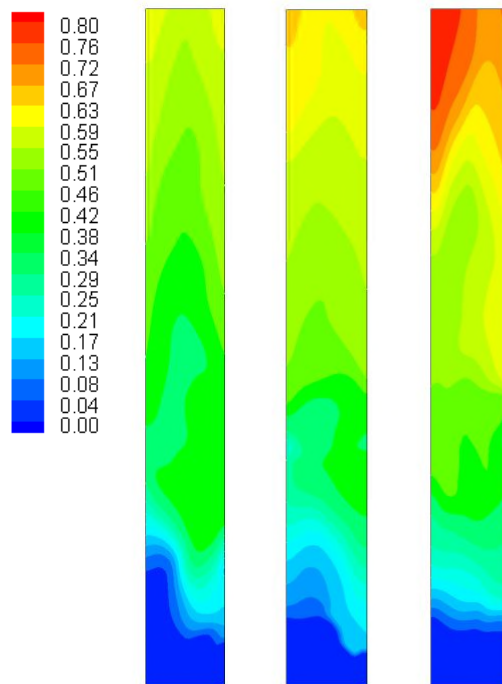
662   (a)   (b)   (c)
663   **Fig. 15 Mass fraction of char in the fluidized bed at 24s: (a) no shrinkage pattern; (b)**
664   **shrinkage pattern 1; (c) shrinkage pattern 2**

665 Figure 15 shows the distribution of the mass fraction of char along the fluidized bed at 24s for the

666 three shrinkage patterns. It can be observed clearly that the mass fraction of char near the outlet

667 increases with the degree of particle shrinkage. This is because the more the particles shrink, the

668 longer their residence time in the reactor, which favours the conversion of lignin towards char. The

669 results shown in Figure 15 are in good agreement with the evidence of the relationship between

670 particle residence time and shrinkage patterns provided in section 4.4.

5. Conclusion

672 In this paper, biomass particle shrinkage in a lab-scale fluidized bed was successfully simulated with a

673 comprehensive CFD model. The state-of-the-art QMOM method for solving the particle PBE was

674 employed, accounting for particle size evolution in the fluidized bed. A 3-parameter shrinkage model

675 was used to calculate the particle shrinking rate as well as the apparent density of the biomass particle.

676 Three different sets of shrinkage factors related to different particle shrinkage patterns were

677 investigated thoroughly to determine how size and density variation affect the main performance

678 parameters of the fluidized bed, such as product yields, char distribution, particle residence time, etc.

679 The degree of shrinkage increases in the sequence of no shrinkage pattern, shrinkage pattern 1 and

680 shrinkage pattern 2, in which the shrinkage factor takes the value of $\alpha=1$, $\beta=1$, $\gamma=1$; $\alpha=1$, $\beta=0$, $\gamma=1$; and

681 $\alpha=0.5$, $\beta=0$, $\gamma=0.5$, respectively.

682 It was shown that for all three cases investigated in this study, the particle apparent density decreases

683 due to continuous mass loss and pore formation. Particle apparent density at the outlet of the fluidized

684 bed drops to 95 kg/m^3, 160 kg/m^3 and 245 kg/m^3 correspondingly from an initial value of 400 kg/m^3.

685 In the no shrinkage case, mass loss of the biomass particle was totally accounted for by pore formation

686 so that a constant size could be maintained, while, in the other two cases, this was only partly

687 accounted for by pore formation, and depends in part on the particle shrinkage. Hence, the particle

688 diameter at the outlet comes to 290μm and 250μm respectively, due to the different percentage of

689 distribution of the aforementioned particle phenomena.

690   An innovative particle tracking technology based on the Eulerian CFD framework is demonstrated in

691   this study to quantitatively estimate the particle residence time. A number of individual particles were

692   consistently tracked from a dynamic update of the flow field. The biomass particle residence time in

693   the dense zone and the whole domain were evaluated statistically with the tracking results. On

694   average these were 2.69s, 3.17s, 4.04s for the dense zone, and 3.96s, 4.6s, 5.73s for the whole domain.

695   The trend of increasing residence time with degree of particle shrinkage also provides a good

696   explanation for the effect of some of the characteristics of the fluidized bed that arise from variations

697   in the particle properties.

698   Different particle shrinkage patterns also have an effect on the devolatilization process of the biomass

699   reactants, especially the percentage of conversion and char distribution. Bio-oil yield seems insensitive

700   to particle shrinkage patterns, at approximately 63%. In contrast, char yield increases slightly with the

701   degree of particle shrinking, from 14.93% for no shrinkage pattern to 17.83% for shrinking pattern 2.

702   This is due to the increasing residence time of biomass particles.

703

704   6. Acknowledgement

708

709   Notations

710   A – frequency factor in the Arrhenius equation (s^{-1})

711   C_p – heat capacity ($kJ \cdot kg^{-1} \cdot K^{-1}$)

712   d – particle diameter (m)

713    $\bar{d}$ – particle number-mean diameter (m)

714    $D_{i,j}$ – mass diffusion coefficient of the jth component in the ith phase (kg·m^{-1}·s^{-1})

715   E – activated energy in the Arrhenius equation (kJ·mol^{-1})

716   e_{ss} – the restitution coefficient

717    $g_{0,ss}$ – the radial distribution function

718   h – phase enthalpy (J·kg^{-1})

719    $h_{i,k}$ – interphase heat transfer coefficient (W·K^{-1}·m^{-3})

720   Δh – enthalpy change (kJ·kg^{-1})

721   I_{2D} – the second invariant of the deviatoric stress tensor

722    $\bar{\bar{I}}$ – unit tensor

723   g – acceleration of gravity (m·s^{-2})

724   k – reaction rate (kg·m^{-3}·s^{-1})

725    $K_{i,j}$ – phase exchange coefficient of momentum (kg·m^{-3}·s^{-1})

726   L – particle size (m)

727   M – mass (kg)

728   m_i – the ith moment of the biomass phase

729    $m_{i,j}$ – mass transfer rate from phase i to phase j (kg·m^{-3}·s^{-1})

730   m_{k^i,i^j} – mass transfer rate per unit volume of the ith component of the kth phase to the jth component

731   of the ith phase (kg·m^{-3}·s^{-1})

732   N – total number of the biomass particle per unit volume

733   Nu – Nusselt number

734   p – pressure (Pa)

735   Pr – Prandtl number

736    $Q_{i,j}$ – interphase heat transfer rate between phase i and phase j (J·m^{-3}·s^{-1})

737   R – volume shrinkage rate (m^3·m^{-3}·s^{-1})

738     $\mathbf{R}_{i,j}$ – drag force between phase i and phase j (N·m⁻³)

739     $\mathrm{R}_{i,j}$ – net producing rate of the jth component in the ith phase (kg·m⁻³·s⁻¹)

740   Re – Reynolds number

741   S – source term of the conservation equations

742   t – time (s)

743   T – temperature (K)

744     $\mathbf{u}$ – velocity vector (m·s⁻¹)

745   V – volume (m³)

746     $x_{i,j}$ – mass fraction of jth component of the ith phase

747   Y – stoichiometric coefficient of char

748   **Greek letters**

749   α – shrinkage factor

750   β – shrinkage factor

751   γ – shrinkage factor

752   ε – volume fraction of a specific phase

753   φ – angle of internal friction

754   λ_s – bulk viscosity of a solid phase (Pa·s)

755   λ_i – phase thermal conductivity coefficient (W·m⁻¹·K⁻¹)

756   λ – species thermal conductivity coefficient (W·m⁻¹·K⁻¹)

757   μ – viscosity (Pa·s)

758     $\mu_{s,col}$ – collision viscosity of a solid phase (Pa·s)

759     $\mu_{s,kin}$ – kinetic viscosity of a solid phase (Pa·s)

760     $\mu_{s,fr}$ – frictional viscosity of a solid phase (Pa·s)

761   ρ – density (kg·m⁻³)

762     $\rho_{apparent}$ – apparent density (kg·m⁻³)

763     $\bar{\bar{\tau}}$ – Stress tensor of a specific phase momentum equation

764   Θ – granular temperature of a solid phase

765   η – reaction progress factor

766   **Subscripts**

767   b – biomass phase

768   c – cellulose

769   h – hemicellulose

770   l – lignin

771   C – char

772   g – gas

773   i – common index of component or phase

774   j – common index of component or phase

775   s – solid, sand

776   W – biomass solid

References

[1] Sawin, J.L., Sverrisson, F., Seyboth, K., Adib, R., Murdock, H.E., Lins, C., Brown, A., Di Domenico, S.E., Kielmanowicz, D., Williamson, L.E. & Jawahar, R., Renewables 2016 Global Status Report. Key findings. A Record Breaking Year for Renewable Energy: New Installations, Policy Targets, Investment and Jobs. Mainstreaming renewables: guidance for policy makers.

[2] Huber, G.W. & Corma, A., 2007. Synergies between bio- and oil refineries for the production of fuels from biomass, *Angewandte Chemie - International Edition* 46(38), 7184–7201.

[3] Zinoviev, S., Muller-Langer, F., Das, P., Bertero, N., Fornasiero, P., Kaltschmitt, M., Centi, G. & Miertus, S., 2010. Next-generation biofuels: Survey of emerging technologies and sustainability issues, *ChemSusChem* 3(10), 1106–1133.

[4] Bridgwater, A.V., 2003. Renewable fuels and chemicals by thermal processing of biomass, *Chemical Engineering Journal* 91(2), 87–102.

[5] Bridgwater, A.V., 1995. The technical and economic feasibility of biomass gasification for power generation, *Fuel*, 74(5), 631–653.

[6] Laird, D.A., Brown, R.C., Amonette, J.E. & Lehmann, J., 2009. Review of the pyrolysis platform for coproducing bio-oil and biochar, *Biofuels, Bioproducts and Biorefining* 3(5), 547–562.

[7] Wright, M.M. & Brown, R.C., 2007. Comparative economics of biorefineries based on the biochemical and thermochemical platforms, *Biofuels, Bioproducts and Biorefining* 1(1), 49–56.

[8] Czernik, S. & Bridgwater, A.V., 2004. Overview of applications of biomass fast pyrolysis oil, *Energy & Fuels* 18(2), 590–598.

[9] Mohan, D., Pittman, C.U. & Steele, P.H., 2006. Pyrolysis of Wood/Biomass for Bio-oil: A Critical Review, *Energy & Fuels* 20(3), 848–889.

[10] Scott, D.S., Majerski, P., Piskorz, J. & Radlein, D., 1999. A second look at fast pyrolysis of biomass—the RTI process, *Journal of Analytical and Applied Pyrolysis* 51(1), 23–37.

[11] Pepiot, P., Dibble, C. J. & Foust, T.D., 2010. Computational fluid dynamics modeling of biomass

802   gasification and pyrolysis, *Computational modeling in lignocellulosic biofuel production. Golden: American Chemical Society*, 273-298.

804   [12] Xue, Q. & Fox, R.O., 2015. Computational Modeling of Biomass Thermochemical Conversion in Fluidized Beds: Particle Density Variation and Size Distribution, *Industrial & Engineering Chemistry Research* 54(16), 4084–4094.

807   [13] Fan, R. & Fox, R.O., 2008. Segregation in polydisperse fluidized beds: Validation of a multi-fluid model, *Chemical Engineering Science* 63(1), 272–285.

809   [14] Kuipers, J. A.M. & van Swaaij, W.P.M., 1998. Computational fluid dynamics applied to chemical reaction engineering, *Advances in Chemical Engineering* 24, 227–328.

811   [15] van der Hoef, M.A., van Sint Annaland, M., Deen, N.G. & Kuipers, J.A.M., 2008. Numerical Simulation of Dense Gas-Solid Fluidized Beds: A Multiscale Modeling Strategy, *Annual Review of Fluid Mechanics* 40(1), 47–70.

814   [16] Authier, O., Ferrer, M., Mauviel, G., Khalfi, A.E. & Lédé, J., 2009. Wood fast pyrolysis: Comparison of Lagrangian and Eulerian modeling approaches with experimental measurements, *Industrial and Engineering Chemistry Research* 48(10), 4796–4809.

817   [17] Lathouwers, D. & Bellan, J., 2001. Yield optimization and scaling of fluidized beds for tar production from biomass, *Energy and Fuels* 15(5), 1247–1262.

819   [18] Lathouwers, D. & Bellan, J., 2001. Modeling of dense gas-solid reactive mixtures applied to biomass pyrolysis in a fluidized bed, *International Journal of Multiphase Flow* 27(12), 2155–2187.

821   [19] Gerhauser, H., Generalis, S.C., Hague, R.A. & Bridgwater, A.V., 2001. CFD for the Modelling of Entrainment in Fluidised Bed Fast Pyrolysis of Biomass, *Progress in Thermochemical Biomass Conversion*, 1281–1295.

824   [20] Gerber, S., Behrendt, F. & Oevermann, M., 2010. An Eulerian modeling approach of wood gasification in a bubbling fluidized bed reactor using char as bed material, *Fuel* 89(10), 2903–2917.

826   [21] Xue, Q., Heindel, T.J. & Fox, R.O., 2011. A CFD model for biomass fast pyrolysis in fluidized-bed reactors, *Chemical Engineering Science* 66(11), 2440–2452.

828 [22] Xue, Q., Dalluge, D., Heindel, T.J., Fox, R.O., & Brown, R.C., 2012. Experimental validation and CFD

829 modeling study of biomass fast pyrolysis in fluidized-bed reactors, *Fuel* 97, 757–769.

830 [23] Mellin, P., Zhang, Q., Kantarelis, E. & Yang, W., 2013. An Euler-Euler approach to modeling

831 biomass fast pyrolysis in fluidized-bed reactors - Focusing on the gas phase, *Applied Thermal*

832 *Engineering* 58(1), 344–353.

833 [24] Mellin, P., Kantarelis, E. & Yang, W., 2014. Computational fluid dynamics modeling of biomass fast

834 pyrolysis in a fluidized bed reactor, using a comprehensive chemistry scheme, *Fuel* 117, 704–715.

835 [25] Ranzi, E., Cuoci, A., Faravelli, T., Frassoldati, A., Migliavacca, G., Pierucci, S. & Sommariva, S., 2008.

836 Chemical kinetics of biomass pyrolysis, *Energy and Fuels* 22(6), 4292–4300.

837 [26] Fletcher, D.F., Haynes, B.S., Christo, F.C. & Joseph, S.D., 2000. A CFD based combustion model of

838 an entrained flow biomass gasifier, *Applied Mathematical Modelling* 24(3), 165–182.

839 [27] Papadikis, K., Gu, S. & Bridgwater, A.V., 2008. CFD modelling of the fast pyrolysis of biomass in

840 fluidised bed reactors, Part A: Eulerian computation of momentum transport in bubbling fluidised

841 beds, *Chemical Engineering Science* 63(16), 4218–4227.

842 [28] Papadikis, K., Gu, S. & Bridgwater, A.V., 2009. CFD modelling of the fast pyrolysis of biomass in

843 fluidised bed reactors: Modelling the impact of biomass shrinkage, *Chemical Engineering Journal*

844 149(1), 417–427.

845 [29] Papadikis, K., Gu, S. & Bridgwater, A.V., 2009. CFD modelling of the fast pyrolysis of biomass in

846 fluidised bed reactors. Part B: Heat, momentum and mass transport in bubbling fluidised beds,

847 *Chemical Engineering Science* 64(5), 1036–1045.

848 [30] Papadikis, K., Gu, S. & Bridgwater, A.V., 2010. Computational modelling of the impact of particle

849 size to the heat transfer coefficient between biomass particles and a fluidised bed, *Fuel Processing*

850 *Technology* 91(1), 68–79.

851 [31] Bruchmülle, J., van Wachem, B.G.M., Gu, S., Luo, K.H. & Brown, R.C., 2012. Modeling the

852 Thermochemical Degradation of Biomass Inside a Fast Pyrolysis Fluidized Bed Reactor, *AIChE Journal*

853 58(10), 3030–3042.

854   [32] Hastaoglu, M.A., Kahraman, R. & Syed, M.Q., 2000. Pellet breakup due to pressure generated

855   during wood pyrolysis, *Industrial & Engineering Chemistry Research* 39(9), 3255–3263.

856   [33] Miller, R.S. & Bellan, J., 1998. Numerical Simulation of Vortex Pyrolysis Reactors for Condensable

857   Tar Production from Biomass, *Energy & Fuels* 12(1), 25–40.

858   [34] Di Blasi, C., 1996. Heat, momentum and mass transport through a shrinking biomass particle

859   exposed to thermal radiation, *Chemical Engineering Science* 51(7), 1121–1132.

860   [35] Villermaux, J., Antoine, B., Lede, J. & Soulignac, F., 1986. A new model for thermal volatilization

861   of solid particles undergoing fast pyrolysis, *Chemical Engineering Science*, 41(1), 151–157.

862   [36] Huang, Q.X., Wang, R.P., Li, W. J., Tang, Y.J., Chi, Y. & Yan, J.H., 2014. Modeling and Experimental

863   Studies of the Effects of Volume Shrinkage on the Pyrolysis of Waste Wood Sphere, *Energy & Fuels*

864   28(10), 6398–6406.

865   [37] Wang, Q., Zhao, Y. & Zhang, Y., 2014. Shrinkage kinetics of large-sized briquettes during pyrolysis

866   and its application in tamped coal cakes from large-scale chambers, *Fuel* 138, 1–14.

867   [38] Fan, R., Marchisio, D.L. & Fox, R.O., 2004. Application of the direct quadrature method of

868   moments to polydisperse gas–solid fluidized beds, *Powder Technology* 139(1), 7–20.

869   [39] Fan, R., Fox, R.O. & Muhle, M.E., 2007. Role of intrinsic kinetics and catalyst particle size

870   distribution in CFD simulations of polymerization reactors, *The 12th International Conference on*

871   *Fluidization-New Horizons in Fluidization Engineering,* 992–1000.

872   [40] Marchisio, D.L. & Fox, R.O., 2005. Solution of population balance equations using the direct

873   quadrature method of moments, *Journal of Aerosol Science* 36(1), 43–73.

874   [41] Passalacqua, A., Fox, R.O., Garg, R. & Subramaniam, S., 2010. A fully coupled quadrature-based

875   moment method for dilute to moderately dilute fluid-particle flows, *Chemical Engineering Science*

876   65(7), 2267–2283.

877   [42] Gidaspow, D., 1994. *Multiphase flow and fluidization: continuum and kinetic theory descriptions*.

878   Academic press.

879   [43] Gidaspow, D., Bezburuah, R. & Ding, J., 1991. *Hydrodynamics of circulating fluidized beds: kinetic*

880   *theory approach* (No. CONF-920502-1). Illinois Inst. of Tech., Chicago, IL (United States). Dept. of

881   Chemical Engineering.

882   [44] Syamlal, M., Rogers, W. & O'Brien, T., 1993. *MFIX Documentation: Volume 1, Theory Guide*.

883   [45] Schaeffer, D.G., 1987. Instability in the evolution equations describing incompressible granular

884   flow, *Journal of Differential Equations* 66(1), 19–50.

885   [46] Lun, C.K.K., Savage, S.B., Jeffrey, D.J. & Chepurniy, N., 1984. Kinetic theories for granular flow:

886   inelastic particles in Couette flow and slightly inelastic particles in a general flowfield, *Journal of Fluid*

887   *Mechanics* 140, 223–256.

888   [47] Syamlal, M., 1987. *The Particle-Particle Drag Term in a Multiparticle Model of Fluidization*, Eg&G

889   Washington Analytical Services Center, Inc., Morgantown, WV(USA).

890   [48] Gunn, D.J., 1978. Transfer of heat or mass to particles in fixed and fluidised beds, *International*

891   *Journal of Heat and Mass Transfer* 21(4), 467–476.

892   [49] Collier, A.P., Hayhurst, A.N., Richardson, J.L., & Scott, S.A., 2004. The heat transfer coefficient

893   between a particle and a bed (packed or fluidised) of much larger particles, *Chemical Engineering*

894   *Science* 59(21), 4613–4620.

895   [50] Curtis, L.J. & Miller, D.J., 1988. Transport model with radiative heat transfer for rapid cellulose

896   pyrolysis, *Industrial & Engineering Chemistry Research* 27(10), 1775–1783.

897   [51] Di Blasi, C., 1993. Analysis of Convection and Secondary Reaction Effects within Porous Solid Fuels

898   undergoing Pyrolysis, *Combustion Science and Technology* 90(5-6), 315–340.

899   [52] Miller, R.S. & Bellan, J., 1996. Analysis of Reaction Products and Conversion Time in the Pyrolysis

900   of Cellulose and Wood Particles, *Combustion Science and Technology* 119(1-6), 331–373.

901   [53] Shafizadeh, F. & Bradbury, A.G.W., 1979. Thermal Degradation of Cellulose in Air and Nitrogen At

902   Low Temperatures, *Journal of Applied Polymer Science* 23(5), 1431–1442.

903   [54] Ward, S.M. & Braslaw, J., 1985. Experimental weight loss kinetics of wood pyrolysis under vacuum,

904   *Combustion and Flame* 61(3), 261–269.

905   [55] Koufopanos, C.A., Lucchesi, A. & Maschio, G., 1989. Kinetic modelling of the pyrolysis of biomass

906   and biomass components, *The Canadian Journal of Chemical Engineering* 67(1), 75–84.

907   [56] Miller, R.S. & Bellan, J., 1997. A Generalized Biomass Pyrolysis Model Based on Superimposed

908   Cellulose, Hemicellulose and Lignin Kinetics, *Combustion Science and Technology* 126(1-6), 97–137.

909   [57] Jin, W., Singh, K. & Zondlo, J., 2013. Pyrolysis Kinetics of Physical Components of Wood and Wood-

910   Polymers Using Isoconversion Method, *Agriculture* 3(1), 12–32.

911   [58] Koufopanos, C.A., Papayannakos, N., Maschio, G. & Lucchesi, A., 1991. Modelling of the Pyrolysis

912   of Biomass Particles. Studies on Kinetics, Thermal and Heat Transfer Effects, *The Canadian journal of*

913   *chemical engineering* 69(4), 907–915.

914   [59] Di Blasi, C., 1994. Numerical Simulation of Cellulose Pyrolysis, *Biomass and Bioenergy* 7(1), 87–98.

915   [60] Randolph, A.D. & Larson, M.A., 1971. *Theory of Particulate Processes*. New York: Academic Press.

916   [61] McGraw, R., 1997. Description of Aerosol Dynamics by the Quadrature Method of Moments,

917   *Aerosol Science and Technology* 27(2), 255–265.

918   [62] Fan, L.T., Fan, L.S., Miyanami, K., Chen, T.Y. & Walawender, W.P., 1977. A Mathematical Model

919   for Pyrolysis of a Solid Particle: Effects of the Lewis Number, *The Canadian Journal of Chemical*

920   *Engineering* 55(1), 47–53.

921   [63] Min, J., Drake, J.B., Heindel, T.J. & Fox, R.O., 2010. Experimental Validation of CFD Simulations of

922   a Lab-Scale Fluidized-Bed Reactor with and without Side-Gas Injection, *AIChE journal* 56(6), 1434–1446.

923   [64] Liu, D. & Chen, X., 2010. Lateral Solids Dispersion Coefficient in Large-scale Fluidized

924   Beds, *Combustion and Flame 157*(11), 2116–2124.

925   [65] Harlow, F.H. & Welch, J.E., 1965. Numerical Calculation of Time‐dependent Viscous

926   Incompressible Flow of Fluid with Free Surface, *The Physics of Fluids 8*(12), 2182–2189.

927   [66] Yeung, P.K. & Pope, S.B., 1988. An Algorithm for Tracking Fluid Particles in Numerical Simulations

928   of Homogeneous Turbulence, *Journal of Computational Physics*, *79*(2), 373-416.

929   [67] Anderson, M.P. & Woessner, W.W., 1992. *Applied Groundwater Modelling*. Academic Press.

930   [68] Genel, S., Vogelsberger, M., Nelson, D., Sijacki, D., Springel, V. & Hernquist, L., 2013. Following

931   the Flow: Tracer Particles in Astrophysical Fluid Simulations, *Monthly Notices of the Royal*

932   *Astronomical Society*, *435*(2), 1426–1442.

933   [69] Federrath, C., Glover, S.C.O., Klessen, R.S. & Schmidt, W., 2008. Turbulent Mixing in the

934   Interstellar Medium: an Application for Lagrangian Tracer Particles. *Physica Scripta*, *2008*(T132),

935   014025.

936   [70] Vazza, F., Gheller, C. & Brunetti, G., 2010. The Mixing and Transport Properties of the Intra Cluster

937   Medium: a Numerical Study Using Tracers Particles, *Astronomy & Astrophysics*, *513*, A32.

938   [71] Patel, M., 2013. *Pyrolysis and gasification of biomass and acid hydrolysis residues* (Doctoral

939   dissertation, Aston University).

940   [72] Di Blasi, C., 2008. Modeling chemical and physical processes of wood and biomass pyrolysis,

941   *Progress in Energy and Combustion Science* 34(1), 47–90.
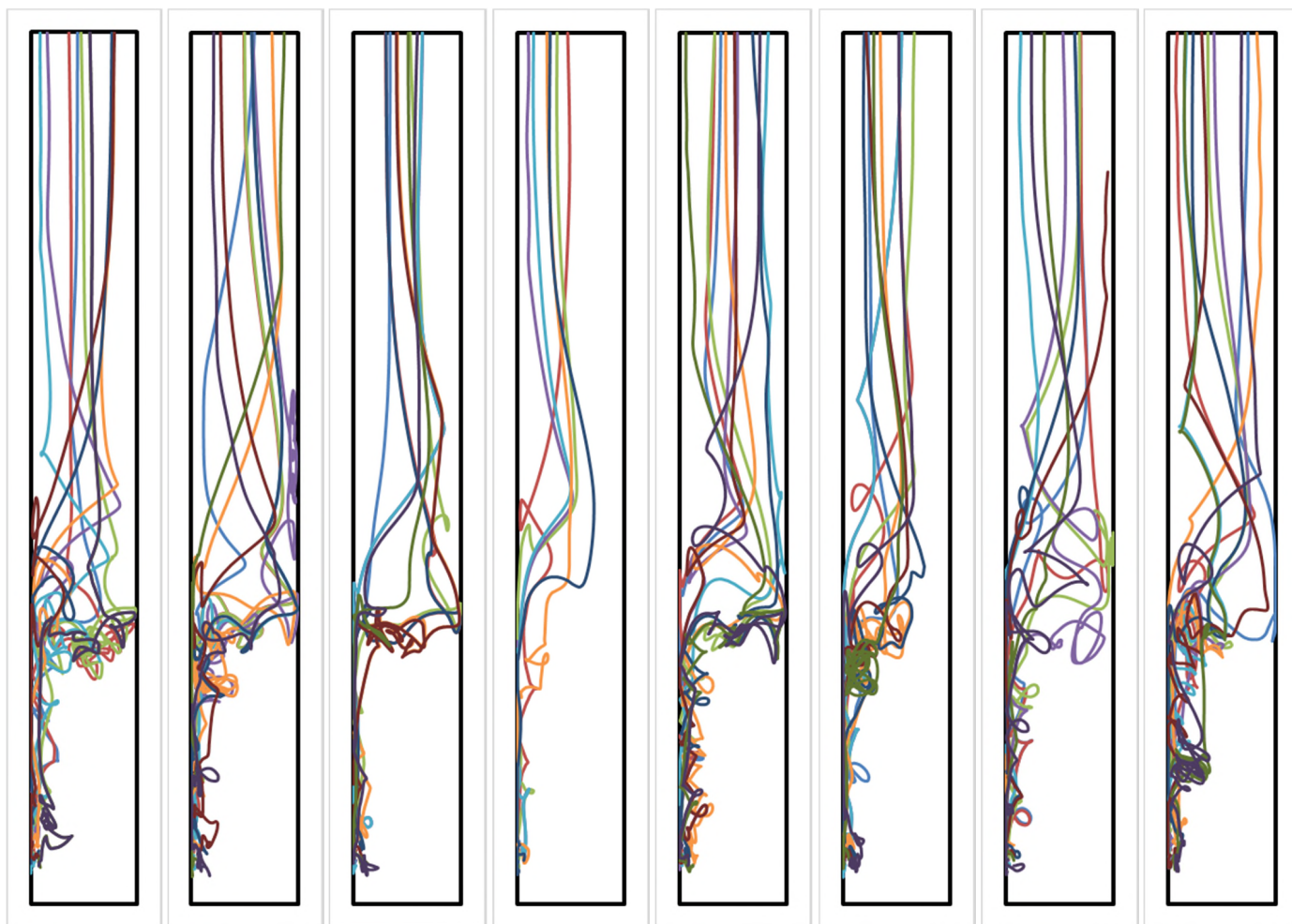
942

943

944

945

946

947

948

949

950   **Appendix**

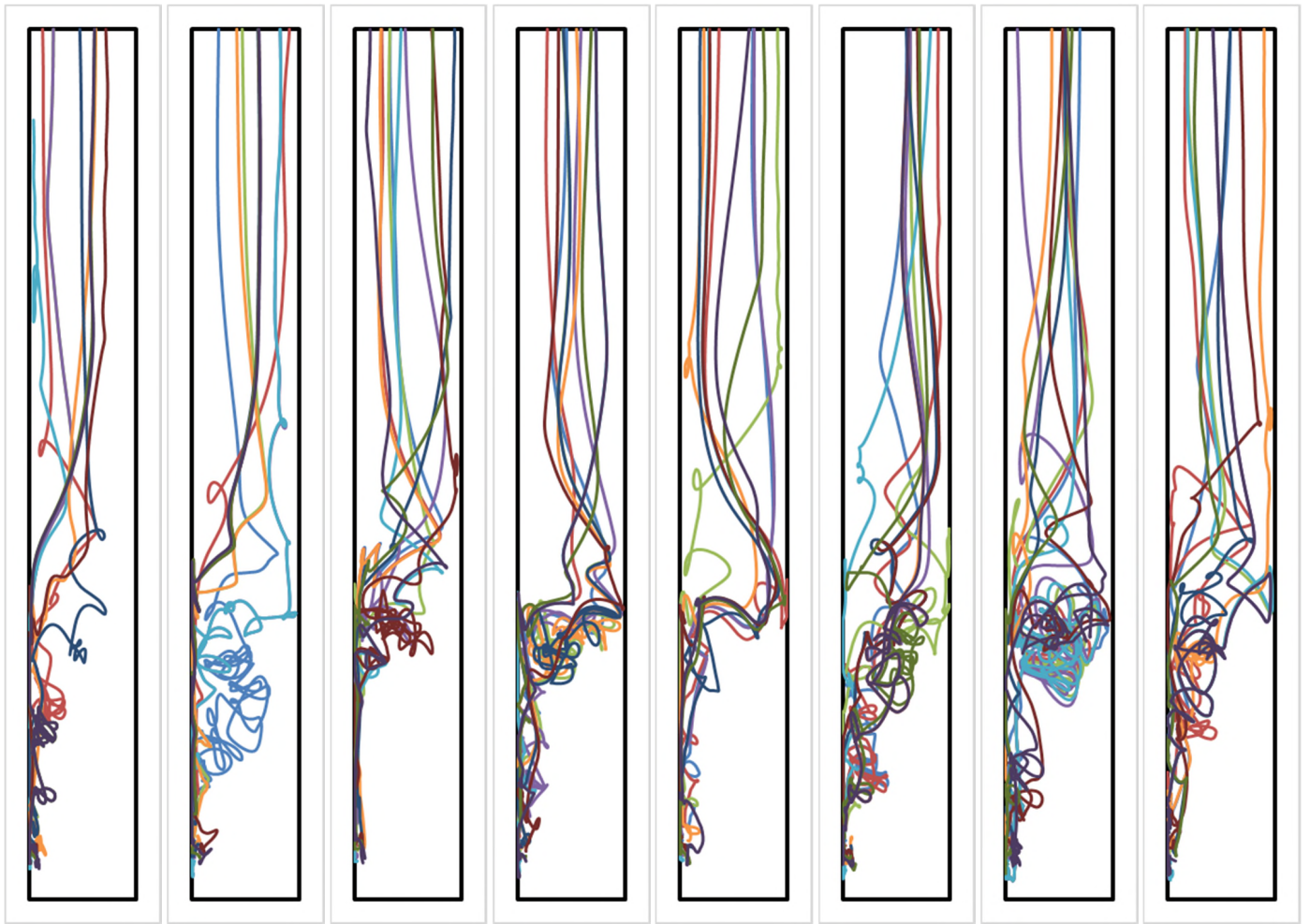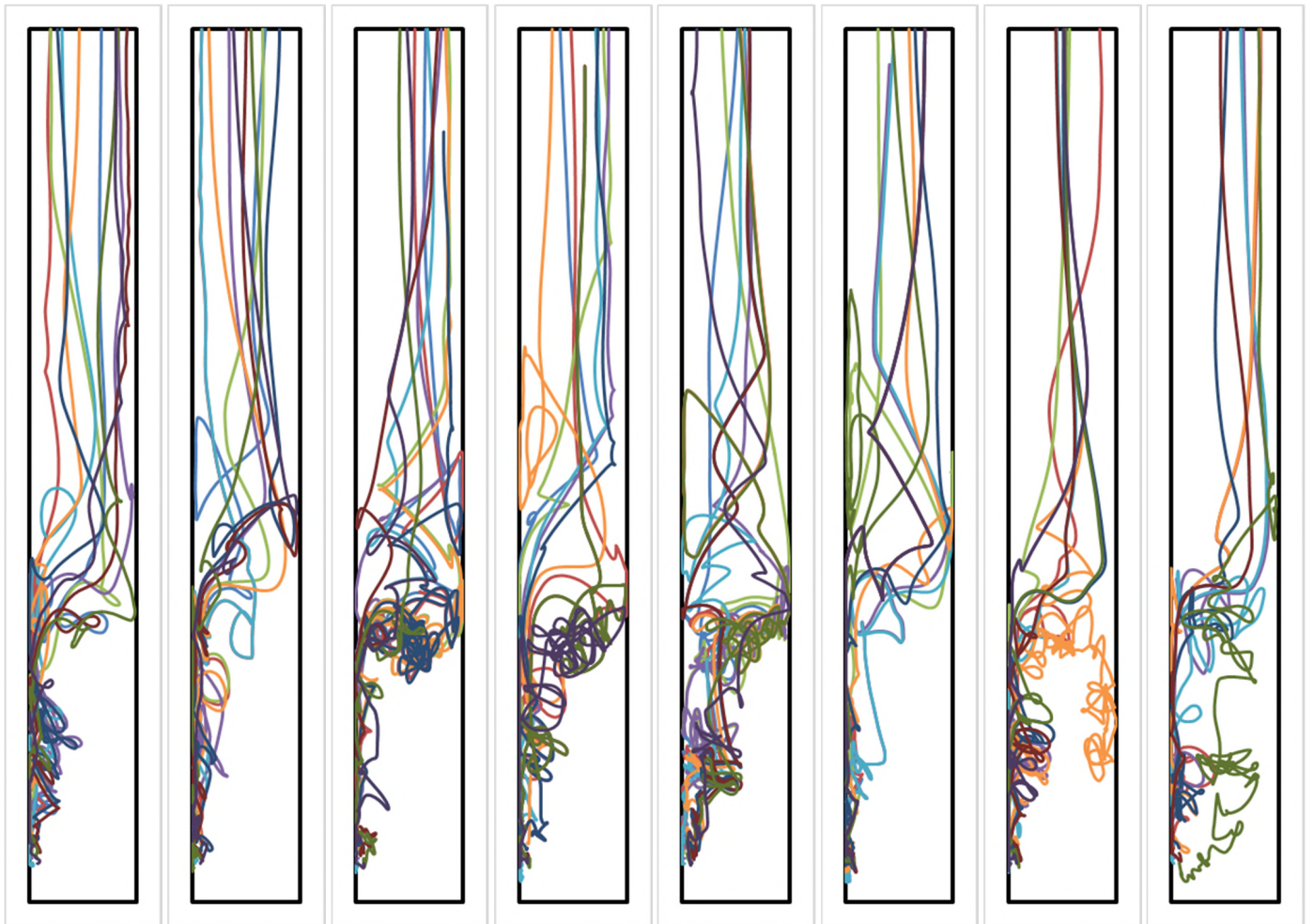951   Some of particle trajectories (10 trajectories generally in each diagram)

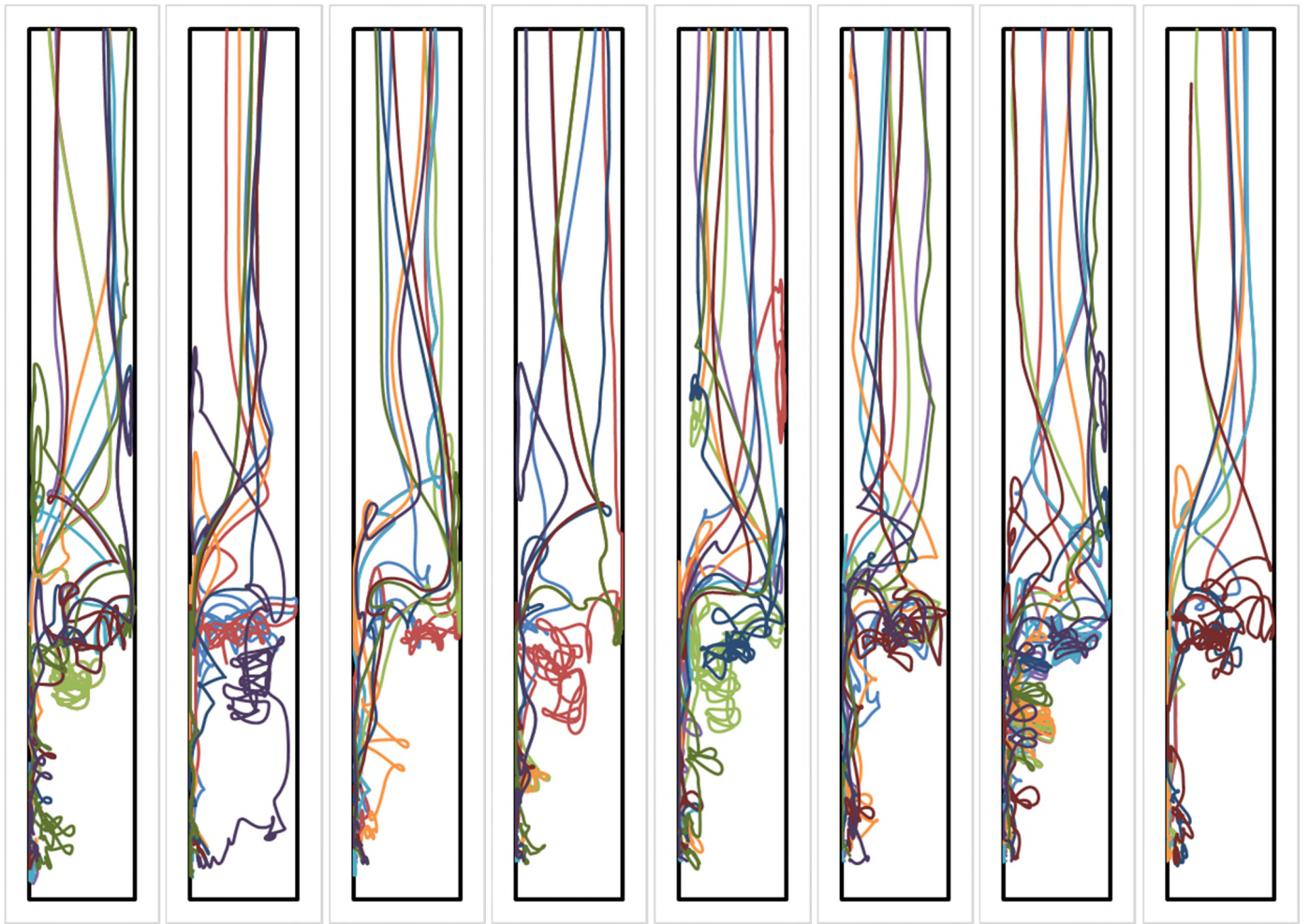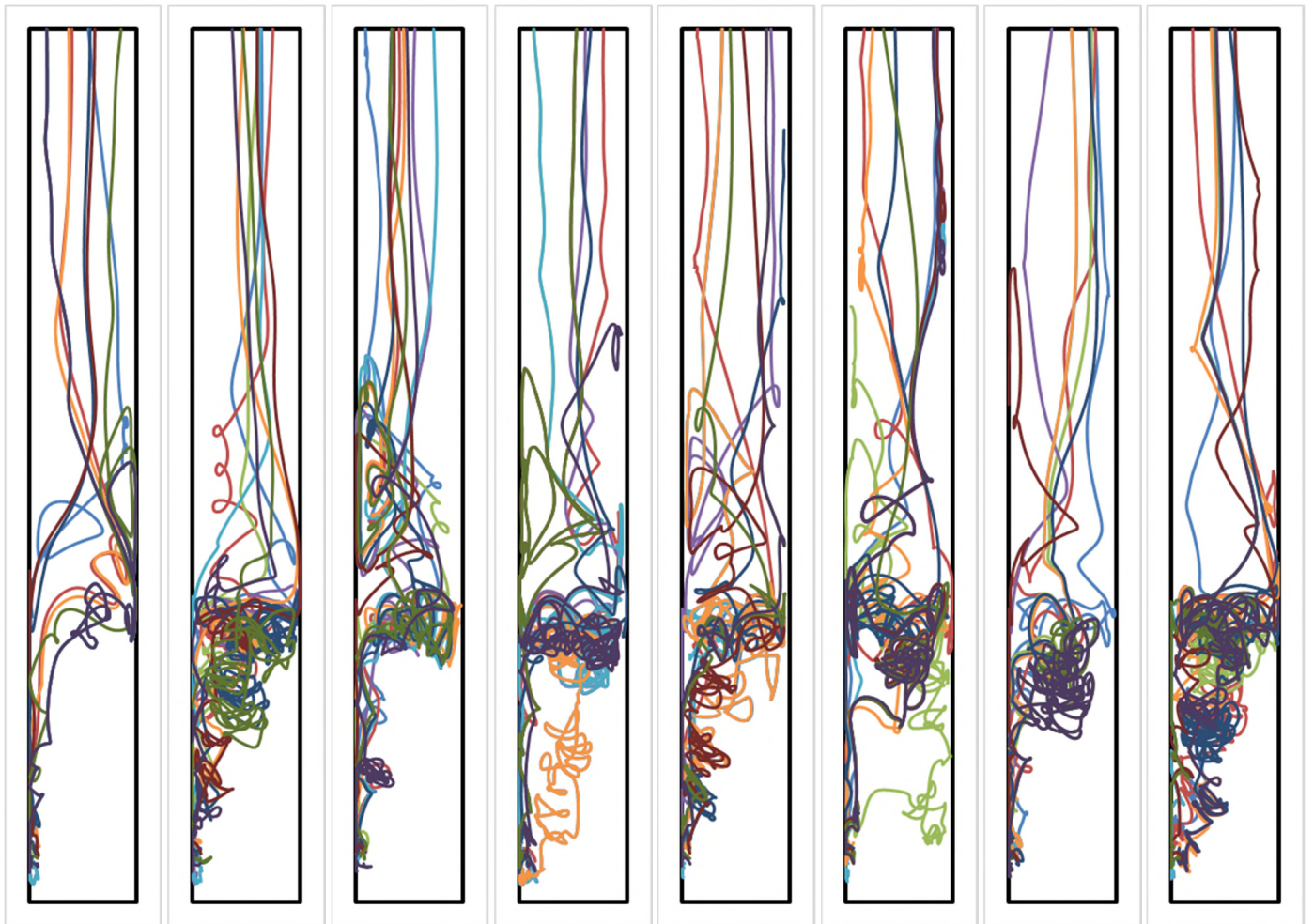**Fig. A.1 Particle trajectories for no-shrinkage pattern**
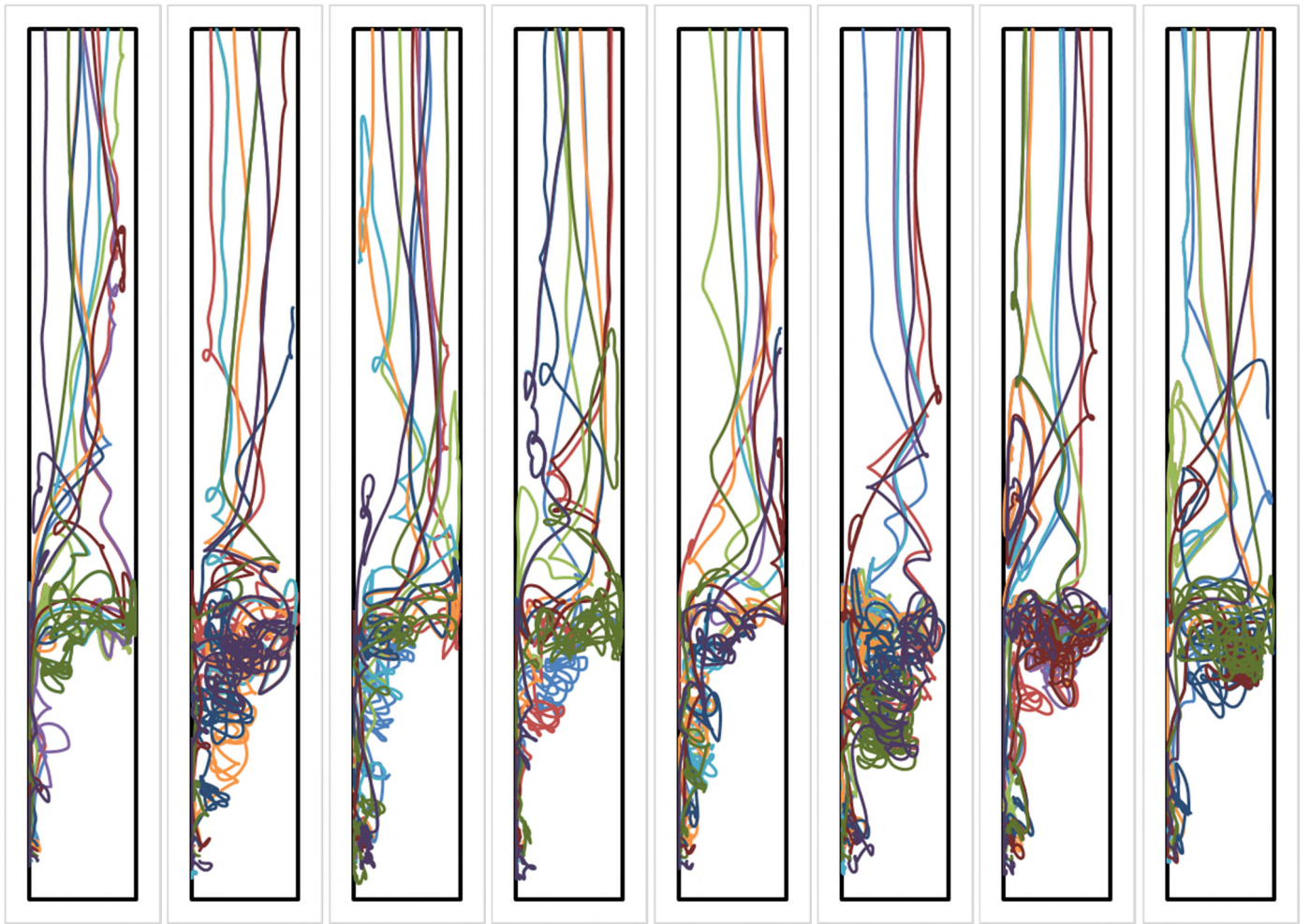
Fig. A.2 Particle trajectories for shrinkage pattern 1

Fig A.3 Particle trajectories for shrinkage pattern 2